
Geochemistry and iron isotope systematics of hydrothermal plume fall-out at East Pacific Rise 9°50'N

Rouxel Olivier ^{1,2,3,*}, Toner Brandy M. ⁴, Manganini Steven J. ¹, German Christopher R. ¹

¹ Woods Hole Oceanog Inst, Woods Hole, MA 02543 USA.

² Ctr Brest, Inst Francais Rech Exploitat Mer, F-29280 Plouzane, France.

³ Univ Hawaii, Dept Oceanog, Honolulu, HI 96822 USA.

⁴ Univ Minnesota, Dept Soil Water & Climate, 1991 Upper Buford Circle, St Paul, MN 55108 USA.

* Corresponding author : Olivier Rouxel, email address : orouxel@hawaii.edu

Abstract :

While gross hydrothermal fluxes entering the ocean are known to be significant, much remains unknown about the fate of this material as it disperses through the oceans, and its impact upon ocean biogeochemistry. Mineral precipitation within hydrothermal plumes removes hydrothermally-sourced metals from solution and also acts to scavenge trace elements from the surrounding water column. Here, we investigate the fate of particulate Fe released from high-temperature hydrothermal venting at EPR 9°50'N and its potential impact on local deep-ocean Fe-isotopic and geochemical budgets. We measured the geochemical composition, mineralogy and Fe isotope systematics of hydrothermal plume products in order to determine whether mineral precipitation imposes characteristic Fe-isotope “fingerprints” for hydrothermally sourced Fe in the deep ocean. Our sampling includes sediment trap deployments after the eruptive event of Jan. 2006, allowing the examination of temporal changes of hydrothermal fluxes over a 160 day period. Results show that Fe isotope composition in the high-temperature vent fluids is rather constant over the sampling period 2004–2008, and that secular variations of $\delta^{56}\text{Fe}$ values of plume particles from -0.03 to -0.91‰ (relative to IRMM-14 standard) could be explained by local processes leading to variable mixing extents of hydrothermal, biogenic and lithogenic particles. Through geochemical modeling, we have calculated the relative abundances of hydrothermal plume components such as sulfides, Fe oxyhydroxides, organic matter, biogenic and lithogenic phases. We demonstrate that Fe isotope fractionation in the hydrothermal plume occurs during the formation and rapid settling of Fe-sulfides that are characterized by $\delta^{56}\text{Fe}$ values ranging from $-0.73 \pm 0.13\text{‰}$ to $-0.86 \pm 0.13\text{‰}$, which is systematically lower than the end-member hydrothermal fluids ($\delta^{56}\text{Fe} = -0.4\text{‰}$). This study suggests that both the initial Fe isotope composition of the high-temperature vent fluids and its initial Fe/H₂S ratio (i.e. Fe-sulfide precipitation versus Fe-oxyhydroxide precipitation) should impose characteristic Fe isotope “fingerprints” for hydrothermally derived Fe in the deep ocean.

Highlights

► Iron isotope composition of hydrothermal vents is fractionated relative to igneous rocks with limited temporal variability ► The relative abundances of hydrothermal plume components are determined using a geochemical model ► Mineral precipitation within hydrothermal plumes impacts local deep-ocean Fe-isotopic budgets

Keywords : Iron isotopes, Seafloor hydrothermal systems, Hydrothermal plume, Marine particles, Sediment traps, Mid-ocean ridges

62

63 **1. Introduction**

64

65 Seafloor hydrothermal activity at mid-ocean ridges (MOR) and ridge-flanks is one of
66 the fundamental processes controlling the exchange of heat and chemical species between
67 seawater and ocean crust (Edmond et al., 1979; Elderfield et al., 1993; Stein and Stein, 1994;
68 Wheat and Mottl, 2000). The interactions between hydrothermal plumes and the surrounding
69 ocean might also significantly impact whole-ocean biogeochemical budgets (Kadko, 1993;
70 Elderfield and Schultz, 1996; German and Von Damm, 2003; German and Seyfried, 2014).
71 Buoyant hydrothermal plumes typically rise $\geq 100\text{m}$ over time-scales of ~ 1 hour, undergoing
72 dilution by $\sim 10,000:1$ with seawater before neutral buoyancy is attained (Lupton et al., 1998).
73 Mineral precipitation within the buoyant plume and the far-field non-buoyant plume removes
74 hydrothermally-sourced metals from solution and also acts to scavenge trace elements from
75 the surrounding water column (Cowen et al., 1986; Cowen et al., 1990; Kadko et al., 1994;
76 Feely et al., 1996; German et al., 1997; Feely et al., 1998). Microbial and geochemical studies
77 have shown that biological productivity and diversity within hydrothermal plumes can be
78 significant, which could be, in part, attributed to CH_4 , NH_4^+ , Mn^{2+} and possibly Fe^{2+} oxidation
79 (Cowen et al., 1986; DeAngelis et al., 1993; Mandernack and Tebo, 1993; O'Brien et al.,
80 1998; Lam et al., 2008; Dick and Tebo, 2010; Bennett et al., 2011a; Sylvan et al., 2012; Dick
81 et al., 2013).

82 It has been commonly considered that dissolved metals were largely removed from
83 hydrothermal plumes through the precipitation of a range of iron-bearing minerals, including Fe-
84 sulfides and Fe oxyhydroxides, and therefore deposited at the seafloor, primarily close to their
85 vent-site sources (Edmond et al., 1982; Mottl and McConachy, 1990; Rudnicki and Elderfield,
86 1993; Klevenz et al., 2011). More recent studies, however, have demonstrated that the
87 contribution of hydrothermal fluxes to the ocean metal budget is not as negligible as originally
88 thought. Research in near-vent settings have identified several mechanisms enhancing the input of
89 hydrothermally sourced metals to the open ocean, including: (i) formation of stable metal-
90 complexes with dissolved and particulate organic carbon (DOC and POC) (Bennett et al., 2008;
91 Toner et al., 2009; Sander and Koschinsky, 2011); (ii) nanoparticulate minerals, in particular
92 pyrite (Yucel et al., 2011; Gartman et al., 2014); (iii) metal uptake by water-column
93 microorganisms (Li et al., 2014). These studies raised fundamental questions regarding the
94 residence time of hydrothermal particles in seawater, their dissolution kinetics and the role of

95 physical and biological processes (Adams et al., 2011; Carazzo et al., 2013). Investigations of far-
96 field vent settings have also highlighted clear hydrothermal contributions for Fe, Mn and probably
97 other metals such as Zn (John and Conway, 2014; Roshan et al., 2016). Long-range transport of
98 hydrothermal Fe has been revealed by mid-water column Fe "anomalies" in the central and south
99 Pacific ocean (Wu et al., 2011a; Fitzsimmons et al., 2014; Resing et al., 2015), the Southern and
100 Artic oceans (Klunder et al., 2012), the equatorial and North Atlantic ocean (Saito et al., 2013;
101 Conway and John, 2014), and the Indian ocean (Nishioka et al., 2013). As a consequence, the
102 global contribution of hydrothermal Fe to the open ocean should be considered in order to balance
103 oceanic Fe budgets (Tagliabue et al., 2010).

104

105 Despite these studies, our current ability to quantify the impact of hydrothermal
106 venting on the deep ocean iron reservoir is far from satisfactory. Since high-temperature vent-
107 fluids define a narrow range in Fe isotope-space slightly lower than igneous rocks, with $\delta^{56}\text{Fe}$
108 values from -0.9‰ to 0.1‰ (Sharma et al., 2001; Beard et al., 2003b; Rouxel et al., 2004;
109 Severmann et al., 2004; Rouxel et al., 2008a; Bennett et al., 2009), it has been hypothesized,
110 previously, that Fe isotope composition may help to better constrain the proportion of
111 hydrothermally-derived deep-ocean dissolved iron. This approach was first proposed for
112 interpreting Fe isotope compositions in hydrogenous crusts (Beard et al., 2003b; Chu et al.,
113 2006; Horner et al., 2015) and later for the Fe isotope composition of seawater (John and
114 Adkins, 2012; Conway and John, 2014). Because Fe-sulfide and Fe-oxide precipitation in
115 hydrothermal plumes can fractionate Fe isotopes toward lighter and heavier values
116 respectively (Severmann et al., 2004; Bennett et al., 2009), it is expected that the Fe isotope
117 composition of any remaining dissolved Fe in seawater will vary significantly depending on
118 the type of minerals formed and the extent of Fe precipitation in the dispersing plume. In
119 addition, the relatively large variations in $\delta^{56}\text{Fe}$ values measured so far in high-temperature
120 hydrothermal fluids compared to other oceanic sources (e.g. rivers, groundwater and
121 diagenetic fluids Bergquist and Boyle, 2006; Severmann et al., 2006; Rouxel et al., 2008b)
122 further complicate the identification of a diagnostic isotopic signature for hydrothermal Fe
123 exported to the ocean.

124

125 Another difficulty is the assessment of the temporal variability of hydrothermal
126 discharge, in particular with respect to volcanic events (Baker et al., 1987; Baker et al., 2012).
127 This is particularly important for Fe since "episodes" of hydrothermal discharge may
128 dominate time-averaged biogeochemical fluxes (Pester et al., 2014). This issue has been

129 generally addressed by examining the chemistry of hydrothermal vents and suspended plume
130 particles overlying hydrothermal fields over repeated periods of time (Baker, 1994; Feely et
131 al., 1994; Breier et al., 2012; Baumberger et al., 2014) and through study of the metalliferous
132 sediments deposited beneath dispersing hydrothermal plumes (Mills and Elderfield, 1995;
133 Cave et al., 2002). Another and more direct approach involves the use of sediment traps to
134 measure *in situ* hydrothermal fluxes over the time frame of weeks to months. Sediment traps
135 have been employed to collect samples in time-series of hydrothermal plume fallout at the
136 Endeavour Segment of the Juan de Fuca Ridge (JdFR) (Dymond and Roth, 1988; Roth and
137 Dymond, 1989; Cowen et al., 2001), 13°N EPR (German et al., 2002) and more recently at
138 EPR 9°50'N (Toner et al., 2009; Adams et al., 2011; Bennett et al., 2011b; Sylvan et al.,
139 2012). In particular, the spatial and temporal variability of vent fluid chemistry at 9°50'N
140 EPR is among the most thoroughly studied of any vent field (Von Damm et al., 1995; Von
141 Damm, 2000; Fornari et al., 2012; Yucel and Luther, 2013). Multiyear time-series of annual
142 to semi-annual sampling at this site have revealed both temporal variability between
143 samplings and differences between vents that are tens of meters apart (Von Damm, 2004;
144 Fornari et al., 2012).

145
146 Here, we investigate the fate of particulate Fe released from high-temperature
147 hydrothermal venting at EPR 9°50'N and its potential impact on local deep-ocean Fe-isotopic
148 and geochemical budgets. We aim to investigate Fe isotope systematics in hydrothermal
149 plume products, formed through Fe-sulfide and Fe-oxyhydroxide precipitation, in order to
150 determine whether mineral precipitation impose characteristic Fe-isotope “fingerprints” for
151 hydrothermally sourced Fe in the deep ocean. Because our sampling includes sediment trap
152 deployments after the eruptive event of Jan. 2006, we also examine temporal changes of metal
153 hydrothermal fluxes in the aftermath of a recent volcanic eruption. Our approach includes
154 calculation of the relative proportions of hydrothermal plume components such as sulfides, Fe
155 oxyhydroxides, organic matter, biogenic and lithogenic components so that the relative
156 contributions of these phases to hydrothermal fluxes and Fe-isotope fractionation can be
157 assessed. Furthermore, we present additional data for Fe isotopes in high-temperature
158 hydrothermal fluids at EPR 9-10°N (Rouxel et al., 2008a) that afford the opportunity to study
159 Fe isotope systematics in vent fluids during the early stage of hydrothermal deposit formation
160 at the seafloor.

161 **2. Materials and methods**

162 ***2.1. Site description and sample selection***

163

164 The hydrothermal field at EPR 9-10°N is located in a well-studied segment of the EPR
165 between the Clipperton and Siqueiros Fracture Zones (Detrick et al., 1987; Haymon et al.,
166 1991; Haymon et al., 1993; Fornari et al., 1998; Shank et al., 1998; Von Damm, 2004). The
167 vent fluid chemistry in the area has been well documented and previous studies have reported
168 temporal evolution of chemical and isotopic properties of the vent systems in relation to
169 magmatic events (Shanks et al., 1995; Von Damm et al., 1997; Shanks, 2001; Von Damm,
170 2004). Eighteen high temperature hydrothermal vent sites have been identified along the EPR
171 between 9°N and 10°N, including ten vent sites between 9°49'N and 9°51'N (**Figure 1**).
172 Hydrothermal activity has ranged from focused discharge of phase-separated high-
173 temperature fluids (up to 403°C) to low-temperature (<20°C) diffuse venting (Von Damm,
174 2004).

175 Since the discovery of vents at 9°50'N, two major eruptions were detected, one in
176 1991/1992 (Haymon et al., 1993) and a second in 2005/2006 (Tolstoy et al., 2006). The
177 former eruption resulted in unprecedented chemical changes, probably related to phase
178 separation and changes in the depth to the heat source driving the hydrothermal system at this
179 site. Those changes were reflected in the variations of temperature as well as Cl and Na
180 contents of the fluids that changed by more than an order of magnitude during this time
181 period (Von Damm et al., 1995; Von Damm et al., 1997; Von Damm, 2000). The latter
182 eruption introduced a major perturbation into local vent communities. New lava emerged
183 between 9°46'N and 9°56'N and reached as far as 2 km off axis (Soule et al., 2007) (**Figure**
184 **1**), covering existing biological communities and even some high-temperature vents. Changes
185 in the iron and sulfide contents and speciation of the high-temperature fluids in the 3 years
186 following the 2005/2006 eruption have been also reported (Yucel and Luther, 2013; Pester et
187 al., 2014).

188

189 We examined descending particles from the buoyant hydrothermal plume near Bio 9
190 (9°50.27N; 104°17.49W) and Tica (9°50.43N; 104°17.49W) vents using 21-position time-
191 series trap sediment traps deployed ~5 m above the seafloor (**Figure 1**). Samples were
192 collected continuously, from May 16 to June 27, 2006 (“RESET” traps “Tica” and “Bio9”),
193 and July 1 to November 4, 2006 (“LADDER 1” trap R1 and R2). The two “RESET” traps

194 near Tica and Bio9 lacked precise navigation and were positioned out of the trough
195 (Mullineaux et al., 2010). Trap R1 was located ~ 30 m southwest of the Bio9 vent complex
196 within the axial summit caldera in an area with a series of small chimneys, black smokers and
197 spires (Von Damm, 2004; Rouxel et al., 2008a). Trap R2 was located outside the axial
198 summit caldera, 115 m southwest of Ty-Io black smoker vents and ~370 m southwest of Trap
199 R1 (**Figure 1**). Following retrieval of Trap R2, it was discovered that a jellyfish had become
200 lodged in the opening at the bottom of the trap during the collection of sample 11 (which
201 began collection on August 30, 2006) and remained there for the duration of the experiment.
202 In this study, we only selected the first 6 samples collected by Trap R2.

203 We also selected several hydrothermal vent fluid samples from the EPR 9°50'N area in
204 order to report geochemical properties of the high-temperature fluid sources prior to mixing
205 with seawater. Vent sites Tica and Bio9 vents were sampled during the Atlantis/Alvin cruise
206 AT11-20 in November 2004 and Fe-isotope compositions together with other chemical
207 characteristics were already reported in (Rouxel et al., 2008a). High temperature fluid
208 samples were also selected after the 2005/2006 eruption for comparison. P-vent, Ty-Io and
209 Bio-9 vent sites were sampled during the Atlantis/Alvin cruise AT15-28 in December
210 2007/January 2008 (Pester et al., 2014). Hydrothermal fluids from Tica vent (344°C) were
211 sampled from large beehive structures while fluids from Bio 9 vents (383°C) were sampled
212 from a typical black smoker chimney.

213

214 ***2.2. Sediment trap samples***

215 The sediment traps (McLane Parflux Mark 78H-21; McLane Research Laboratories)
216 have a sampling aperture of 0.5 m² (80 cm diameter at top, 2.5 cm diameter at bottom) and 21
217 cups. Prior to deployment, each 250 mL polyethylene sample cup was filled with 20%
218 dimethyl sulfoxide (DMSO) in 4.0% NaCl solution and buffered to pH 9.0 ± 0.5 with NaOH.
219 This preservative stops significant biological activity within the samples, retaining sample
220 integrity for mineralogical, geochemical, and molecular microbiological investigations. The
221 use of DMSO, however, prevents the robust analysis of sulfur concentration in plume
222 particles. Upon trap recovery, each sample cup was capped and refrigerated at 4 °C.
223 Subsamples for mineralogy were collected in a laminar flow hood using sterile plastic pipettes
224 after vigorous shaking. Subsequently, all sample processing in the laboratory, including
225 splitting and filtration, was conducted using standard methods established for sediment trap
226 analyses (Honjo et al., 1995). Particulate samples were first water-sieved through 1-mm mesh

227 and < 1mm fractions were further split into 10 equal aliquots using a McLane WSD-IO
228 rotating wet-sediment splitter. Only the < 1 mm fraction was analyzed for the “RESET” traps
229 while both fractions (> 1 mm and < 1 mm) were recovered and analyzed for the “LADDER
230 1” trap. Because of the small amounts of materials recovered in the RESET traps,
231 geochemical analyses were completed on pooled samples by combining the materials from 3
232 or 4 consecutive cups.

233 Total dry mass for mass flux calculations was determined by summing three fractions
234 of the < 1 mm sample splits. The standard error determined from dividing all < 1 mm samples
235 was generally better than 4% (Honjo et al., 1995). Mass flux calculations for > 1 mm samples
236 were done directly by weighting the totality of particles recovered. Subsequent geochemical
237 analyses were done on dried subsamples obtained after 0.4 μm filtration. Between 5 to 10 mg
238 of dried subsamples were analyzed for particulate inorganic carbon (PIC) using a UIC
239 Coulometric analyzer and total particulate carbon (TOC) using a CHN analyzer. Particulate
240 organic carbon (POC) was determined by difference.

241 The larger (> 1 mm) and fine (< 1 mm) fractions of the traps were measured for major
242 element concentrations (Al, Ba, Ca, Fe, Mg, Mn, Si, Sr and Ti) by ICP-OES (Jobin Yvon) at
243 WHOI after complete dissolution using lithium metaborate fusion and final dilution into 20-
244 40 mL of 0.28 M HNO_3 . Accuracy was within 3% as determined by repetitive measurements
245 of a standard (USGC marine sediment MAG-1). Trace element analyses (P, V, Co, Cu, Zn)
246 were done on the same solutions after an additional dilution and analyzed by high-resolution
247 ICPMS Element 2 (Thermo Scientific) at WHOI. The detection limit was calculated from
248 repeat analysis of procedural blanks. Indium was added to each sample as an internal standard
249 to correct for changes in instrument sensitivity. Stock standards (Specpure, Spex) of each
250 element of interest were diluted in preparation for instrument calibration. A number of geo-
251 reference standards (BHVO-1 and IFG) were also analyzed along with the samples to
252 determine analytical accuracy, which is better than 5% for all trace elements reported.

253

254 ***2.3. Hydrothermal fluids***

255 Eight hydrothermal fluids from four active vents were collected by submersible Alvin
256 (WHOI) using two types of pressurized, piston driven sampling devices, made entirely of
257 titanium. Samples recovered using the 'Major' samplers (Von Damm et al., 1985) were
258 previously described in Rouxel et al. (2008a) while samples recovered using the 'IGT'
259 samplers (Seewald et al., 2002) were partly reported in Pester et al. (2014). Briefly, the Ti-

260 samplers were filled via a titanium snorkel that was inserted directly into the vent orifice.
261 Importantly, the snorkel was adapted to contain a thermocouple with ICL communication,
262 which permitted monitoring vent fluid temperature in the course of sampling, effectively
263 minimizing seawater entrainment. Immediately following recovery, fluid pH was measured
264 onboard ship. Several fluid aliquots were extracted from the Ti-samplers and transferred into
265 acid cleaned bottles and acidified with ultrapure HCl. Due to the high concentrations of
266 metals in the hydrothermal solutions, precipitation often occurred within the titanium samplers
267 as they cooled to ambient temperature. These insoluble or precipitated particles were also
268 recovered for chemical analysis by rinsing the disassembled Ti-sampler with Milli-Q water
269 and acetone and filtering the resultant 'dregs' through 0.45 μm filters. Based on the total
270 volume of the sampler, the amount of metals measured in this 'dregs' fraction was recombined
271 with data obtained for the dissolved fraction in order to calculate the original *in situ*
272 composition of the vent fluid samples. The fluid samples were stored acidified for about 6
273 months before analysis. In some cases, suspended particles remaining in the acidified bottles
274 (presumably sulfides) were filtered through 0.2 μm filters. Both 'dregs' and suspended fluid
275 particles were digested with distilled concentrated HNO_3 and HCl, evaporated and analyzed
276 using the same procedure as for fluid samples.

277 For 'Major' fluid samples, Na and Mg concentrations were determined by ion-
278 chromatography while trace elements (Fe, Cu, Mn, Zn) were determined by high-resolution
279 ICPMS Element 2 (Thermo Scientific) as described in Rouxel et al. (2008a). For 'IGT' fluid
280 samples, Na and Mg concentrations were determined by ion-chromatography while trace
281 elements (Fe, Cu, Mn, Zn) were determined by ICP-OES as described in Pester et al. (2011).
282

283 **2.4. Fe isotope analysis**

284 Fe-isotope ratios were determined at WHOI and IFREMER on a Thermo Scientific
285 Neptune MC-ICPMS following the method described in Rouxel et al. (2008a). A portion of
286 the fluid samples, including both the dissolved fraction and the digested 'dregs' fraction was
287 dried down in PTFE beakers on hot plates with 1 mL of concentrated HNO_3 (ultrapure grade).
288 The dry residue was then dissolved with 4 mL of 6 M HCl and a trace of H_2O_2 . Similarly, a
289 portion of the dissolved samples obtained after LiBO_3 fusion was first dried down in PTFE
290 beakers with concentrated HNO_3 . After further evaporation in HNO_3 -HF mixtures, the solid
291 residue was dissolved in 6 M HCl. In general, between 1 μg to 100 μg of Fe were processed
292 through the entire chemical purification. Each sample in 6 M HCl was loaded onto AG1-X8

293 chromatographic resin. The iron fraction was collected after elution with 0.24 M HCl, dried
294 down, re-dissolved in 0.28 M HNO₃ and analyzed on a Neptune ICP-MS as described
295 elsewhere (Rouxel et al., 2008a; Escoube et al., 2009).

296 Our analytical technique on the Neptune MC-ICP-MS at WHOI and IFREMER involves
297 both "sample-standard bracketing" and "internal normalization" using Ni of known isotope
298 composition. It yields an external precision better than 0.07‰ (2σ) for total quantities of
299 Fe down to 500 ng. Based on > 50 replicate dissolutions, purifications and analyses of
300 internal standard BHVO-1 and BHVO-2 (Hawaiian basalt), we have obtained a long-term
301 average of $\delta^{56}\text{Fe} = 0.09 \pm 0.07\text{‰}$ (2σ). We also measured the Fe isotope composition of
302 synthetic seawater-like matrices by adding known amounts of a Fe standard solution (Spex
303 solution) to Fe-depleted seawater to obtain a final Fe concentration similar to hydrothermal
304 fluids. Throughout, we obtained an average $\delta^{56}\text{Fe}$ value of $-0.19 \pm 0.09\text{‰}$ (2sd, n=10)
305 indistinguishable from the values obtained for the pure standard solution. We also measured
306 several aliquots of MAG-1 georeference materials (marine sediment) processed in a similar
307 manner to the sediment trap particles (i.e. digestion using LiBO₃ fusion) and obtained an
308 average $\delta^{56}\text{Fe}$ value of $0.08 \pm 0.09\text{‰}$ (2sd, n=5) similar to the expected values for lithogenic
309 marine sediments (Beard et al., 2003a).

310

311 **2.5. X-ray microprobe**

312 Iron speciation was measured by Fe 1s X-ray absorption near edge structure (XANES)
313 spectroscopy in fluorescence mode at the hard X-ray microprobe beamline 10.3.2 (Manceau
314 et al., 2002; Marcus et al., 2004), Advanced Light Source (ALS), Lawrence Berkeley
315 National Laboratory, Berkeley, CA using methods previously published for EPR plume
316 materials (Toner et al., 2009; Breier et al., 2012). The application of these tools to plume
317 particles was reviewed by Toner et al. (2014; 2016). Briefly, the monochromator was
318 calibrated by setting the inflection point of an Fe 1s XANES spectrum, collected from an Fe
319 foil, to 7110.75 eV (Kraft et al., 1996). The distribution of elements in particles on filters
320 (polycarbonate 0.2 μm) was determined by micro-focused X-ray fluorescence (μXRF)
321 mapping using a 7-element Ge solid-state fluorescence detector (Canberra). XRF map
322 measurements used a $3 \times 3 \mu\text{m}^2$ beam spot on the sample and were used to find sample
323 locations for point Fe XANES data collection. Iron 1s XANES spectra were used to survey
324 the oxidation state and mineral class of the Fe-bearing phases (Toner et al. 2012). Linear

325 combination fitting (LCF) of XANES spectra was performed using a library of standards
326 (Marcus et al., 2008) and custom beamline software (Marcus et al., 2004). The best LCF was
327 chosen based on the normalized sum square parameter (NSS):

$$328 \quad NSS = 100 \times [\sum (\mu_{exp} - \mu_{fit})^2 / \sum (\mu_{exp})^2] \quad (1)$$

329 where the addition of a spectral component to the fit required a 10 % or greater improvement
330 in the NSS value. Best LCF results are provided in the supplemental materials (**Table S1**).
331 Fits to specific reference materials were later binned into broad mineralogical/speciation
332 categories using the key presented in **Table S2**.

333

334 **3. Results and discussion**

335

336 ***3.1. Hydrothermal vent fluids***

337 The hydrothermal fluids collected from P-vent, Bio9, Tica, Ty-Io and Biovent sites
338 (**Table 1**) display a significant range in temperature (331 to 383 °C), salinity (Na
339 concentrations between 228 to 389 mM), and Fe concentrations (from 156 μM at Bio vent to
340 3280 μM at P vent). The low-Mg contents (below 6 mM) for most of the high-temperature
341 hydrothermal fluids reflect minimal dilution with seawater (Mg=53 mM). In some cases,
342 hydrothermal fluids with Mg contents up to 25 mM (e.g. Biovent) were obtained suggesting
343 significant entrainment of seawater during sampling.

344 End-member Fe concentrations and Fe isotope compositions are also reported in
345 **Table 1**. For most samples, the dissolved fraction represents more than 90% of the total Fe,
346 suggesting that the dregs represent a minor fraction. Hence, potential entrainment of small
347 pieces of the sulfide chimney is not expected to affect Fe concentrations and Fe isotope ratios
348 of the end-member vent fluids reported here. Triplicate analyses of P vent fluids sampled in
349 2008 yield an average Fe concentration of $3143 \pm 166 \mu\text{M}$ (1se) and identical $\delta^{56}\text{Fe}$ values of
350 $-0.41 \pm 0.09\text{‰}$ (2sd, n=3). As previously reported by Pester et al. (2014), end-member Fe
351 concentrations at Bio9 showed a marked decrease between 2004 and 2008, with values
352 decreasing from 3584 ± 71 in 2004 (Rouxel et al., 2008a) to $2750 \pm 120 \mu\text{M}$. Despite the
353 change in end-member Fe concentrations, $\delta^{56}\text{Fe}$ values for the Bio 9 vent fluids show a
354 remarkable homogeneity between 2004 and 2008, yielding an overall $\delta^{56}\text{Fe}$ value at $-0.41 \pm$

355 0.04‰ (2sd, n=4). This value is also indistinguishable from P-vent values located close by.
356 As reported by Rouxel et al. (2008a), Fe isotope values at Tica vent differ significantly from
357 other vent sites at EPR 9°50'N with $\delta^{56}\text{Fe}$ values (averaging $-0.36 \pm 0.07\%$, 2sd) that are
358 slightly lower than the nearby Bio 9 vent site. In addition, Tica vent fluids display the largest
359 differences between dissolved and precipitated (i.e. 'dregs' fraction) Fe pools, with
360 $\Delta\delta^{56}\text{Fe}_{\text{Particles-Fluid}}$ ranging from -1.38 to -1.57‰.

361 The single analysis of Ty-10 vent fluids shows much lower Fe concentrations than P
362 vent and Bio9, with end-member values at 583 μM . Ty-10 also yields the heaviest $\delta^{56}\text{Fe}$
363 values at $-0.22 \pm 0.11\%$. Bio vent, located at the northern limit of the study area (**Figure 1**),
364 displays even lower Fe concentrations (290 μM) but lighter $\delta^{56}\text{Fe}$ values at about -0.66% .
365 Hence, vent sites showing the lowest Fe concentrations yield the largest range of $\delta^{56}\text{Fe}$ values,
366 with a total range of about 0.4 ‰. Because these vents are both located away from the
367 sediment traps and contain relatively low Fe concentrations, it is to be expected that their
368 contribution to the total input of hydrothermal Fe recorded in our sediment trap records is
369 negligible.

370

371 So far, all reported high-temperature ($>300^\circ\text{C}$) vent-fluids have been characterized by
372 a range in Fe isotope compositions that is systematically shifted toward light $\delta^{56}\text{Fe}$ values
373 compared to igneous and mantle rocks. Values as low as -0.67% and as high as -0.09%
374 were previously reported in hydrothermal vent fluids along the Mid-Atlantic Ridge and East
375 Pacific Rise (Sharma et al., 2001; Beard et al., 2003b; Severmann et al., 2004; Rouxel et al.,
376 2008a; Bennett et al., 2009). Heaviest values were found for high-temperature hydrothermal
377 fluids from the Rainbow field, an ultramafic-influenced hydrothermal system from the Mid-
378 Atlantic Ridge (Severmann et al., 2004) while lighter values were reported for Fe-depleted
379 vents from basaltic-hosted vent sites at EPR 9°50'N (e.g. Bio-vent, Rouxel et al., 2008a). In
380 general, high-temperature hydrothermal fluids from basaltic-hosted fields exhibit a restricted
381 range from -0.3 down to -0.5‰ (Rouxel et al., 2008a; Bennett et al., 2009).

382

383 Potential processes controlling the variability of Fe isotopes in hydrothermal fluids at
384 fast spreading ridges include phase separation, high-temperature basalt alteration, and
385 subsurface processes leading to Fe precipitation or remobilization below the seafloor. Although
386 phase separation is one of the fundamental processes controlling mid-ocean ridge vent fluid
387 chemistry (Von Damm, 1988; Von Damm et al., 1995), several lines of evidence suggest that

388 only limited Fe-isotope fractionation occurs during this process. First, Beard et al. (2003b)
389 measured $\delta^{56}\text{Fe}$ values of both the vapor and brine phases from the Brandon Vent at EPR
390 21.5°S and found less than 0.15‰ difference between these two fluids. Secondly, although
391 not spatially related, Fe isotope compositions of the high salinity fluid at K-vent (i.e. Na
392 above seawater) do not differ significantly from lower salinity, vapor-rich fluids at Tica vent
393 (Rouxel et al., 2008a). Thirdly, recent experimental studies of Fe isotope fractionation during
394 phase separation in the NaCl-H₂O system (Syverson et al., 2014) yielded a maximum Fe
395 isotope fractionation between the vapor and liquid of $0.15 \pm 0.05\%$ with, in most cases,
396 variations of $\delta^{56}\text{Fe}$ values that were indistinguishable within analytical uncertainties.
397

398 After the 2005/2006 eruption, hydrothermal vent fluids from Bio9 experienced an
399 increase in dissolved Fe concentrations and a depletion in acid-volatile sulfide (i.e. free
400 sulfide plus FeS) concentrations (Yucel and Luther, 2013). Chromium reducible sulfide (i.e.
401 suspended pyrite) was also depleted, probably reflecting much lower Fe/H₂S ratios in the vent
402 fluids following the eruption, due to the formation of an H₂S-laden vapor phase. Time series
403 data for vent fluid chemistry at Bio9 also show an increase in Fe solubility relative to Mn in
404 the aftermath of the volcanic eruptions in both 1991/1992 and 2005/2006 (Pester et al., 2014).
405 This is consistent with experimental data suggesting a sharp increase in Fe solubility in low-
406 salinity and low-density vapor fluids that are associated with eruptive events (Pester et al.,
407 2014). Despite these dramatic changes in end-member Fe chemistry, $\delta^{56}\text{Fe}$ values of Bio 9
408 vent fluids show a remarkable homogeneity between 2004 and 2007/2008, yielding an overall
409 $\delta^{56}\text{Fe}$ value of $-0.41\% \pm 0.04$ (2sd, n=4). One interpretation of these data could be that the
410 system returned to steady state after only 1 year following the major magmatic events, but
411 this would be in contradiction with other studies suggesting a period of 2 to 3 years for
412 recovery after an eruption (Yucel and Luther, 2013; Pester et al., 2014). Alternately, it could
413 be considered that magmatic events do not significantly change the Fe isotope composition of
414 end-member high-temperature vent fluids. Relative to steady state, eruptions can result in a
415 temporary shallowing of the heat source, leading to intersection of the two-phase boundary at
416 lower P-T conditions. However, the lack of significant Fe isotope fractionation during phase
417 separation should not result in large changes of $\delta^{56}\text{Fe}$ values in the resulting vent fluids.

418 Hence, the general enrichment in light Fe isotopes in vent fluids relative to volcanic
419 rocks can be explained by two alternate mechanisms (Rouxel et al., 2003; Rouxel et al., 2004;
420 Rouxel et al., 2008a):

421 (1) high-temperature alteration of basalt and the formation of isotopically heavy secondary
422 minerals (e.g. Mg–Fe amphibole) in the high-temperature reaction zone. This mechanism has
423 been observed already during low-temperature alteration of basalts at the seafloor (Rouxel et
424 al., 2003). In particular, highly altered basalts that are depleted in Fe by up to 80% from their
425 original Fe concentration display an increase in $\delta^{56}\text{Fe}$ values relative to fresh values (up to
426 1.3‰), which suggests preferential leaching of light Fe isotopes (between -0.5‰ and -1.3‰)
427 during alteration.

428 (2) precipitation of isotopically heavy pyrite in subsurface environments or in the reaction
429 zone. Using first-principles methods based on density-functional theory (DFT) and
430 Mössbauer spectroscopy methods, previous theoretical studies have demonstrated that pyrite
431 should be enriched in heavy Fe isotopes under equilibrium conditions (Blanchard et al., 2009;
432 Polyakov and Soultanov, 2011; Blanchard et al., 2012). Using the reduced isotopic partition
433 function ratios of FeS_2 and Fe(II)-aquo-chloro complexes, the isotope fractionation between
434 FeS_2 and Fe(II)aq $\Delta\delta^{56}\text{Fe}_{\text{FeS}_2\text{-Fe(II)}}$ is about 1.0 to 1.5 at 350 °C. Experimentally determined
435 equilibrium pyrite–fluid Fe isotopic fractionation also agrees with theoretical and spectrally-
436 based predictions (Syverson et al., 2013). Under hydrothermal conditions (300–350°C, 500
437 bars) in NaCl- and sulfur-bearing aqueous fluids, $\Delta\delta^{56}\text{Fe}_{\text{FeS}_2\text{-Fe(II)}}$ was determined at $0.99 \pm$
438 0.29‰ (Syverson et al., 2013). Hence, in the case of pyrite precipitation in subsurface
439 environments due to conductive cooling of the fluids, near equilibrium Fe-isotope
440 fractionation is expected which should result in the preferential partitioning of isotopically
441 light Fe in the hydrothermal fluids. This suggests that pyrite acts as an important mineral
442 buffer in the iron isotope composition of high-temperature hydrothermal fluids.
443

444 **3.2. Mass fluxes**

445 The mass flux (in $\text{mg}/\text{m}^2/\text{d}$) together with the chemical composition for each cup are
446 reported in **Table 2** and compared with previous studies at EPR 13°N in **Table 3**. Because the
447 mass fluxes measured for each cup represent an integration of collected materials over a
448 relatively short period of 6 days, we also calculated the fluxes and chemical compositions of
449 each sediment traps integrating the entire duration of deployment (**Table 3**). This approach
450 allows discussion of both short-term evolution and longer temporal records of mass flux and
451 chemical compositions for sinking plume particles.

452 The fluxes measured in trap R1 (period between 07/01/2006 to 11/03/2006) ranged
453 from 0.46 to 2.96 $\text{mg}/\text{cm}^2/\text{yr}$ for $< 1\text{mm}$ fractions and from 0.34 to 2.36 $\text{mg}/\text{cm}^2/\text{yr}$ for > 1

454 mm fractions. This yields an integrated flux for trap R1 of 2.6 mg/cm²/yr, with fluxes from >
455 1mm and < 1mm fractions contributing equally. This flux is comparable to far-field (i.e. 300
456 m away) mass fluxes measured at EPR 13°N (2-3 mg/cm²/yr, German et al., 2002) but lower
457 than near vent (i.e. 10-20 m) mass fluxes (6-16 mg/cm²/yr, German et al., 2002) (**Table 3**).
458 Trap R1 is located ~ 30 m southwest of the Bio9 vents complex within the axial summit
459 caldera suggesting lower hydrothermal input at EPR 9°50'N compared to 13°N. The fluxes
460 are only slightly higher than open-ocean mesopelagic fluxes (0.5 - 1.1 mg/cm²/yr) measured
461 in the North Central Pacific (Lamborg et al., 2008) and off-axis from the Juan de Fuca Ridge
462 (Cowen et al., 2001).

463 The fluxes measured in trap R2 (period between 07/01/2006 to 08/06/2006) range
464 from 0.53 to 1.08 mg/cm²/yr for < 1 mm fractions and from 0.08 to 0.29 mg/cm²/yr for > 1
465 mm fractions. This yields an integrated flux for trap R2 of 0.98 mg/cm²/yr, with fluxes from <
466 1mm fraction contributing more than 80% of the total flux. This mass flux is also much
467 lower than the far-field fluxes measured at EPR13°N (German et al., 2002) located 300 m
468 away from a vent site.

469 The fluxes measured in 'Tica' and 'Bio9' traps between 05/16/2006 to 06/27/2006 are
470 remarkably similar (0.54 and 0.53 mg/cm²/yr, respectively). Because only the < 1 mm
471 fraction was recovered, it is impossible to determine whether the missing > 1 mm fraction
472 contributed significantly to the total mass flux. According to our results for R1 and R2 traps,
473 the > 1 mm fraction can contribute from 20% to 50% of the total mass flux, suggesting that
474 our mass fluxes for the 'Tica' and 'Bio9' traps are significantly underestimated. In all cases,
475 however, mass fluxes of about 0.5 mg/cm²/yr for the < 1 mm fraction are surprisingly low,
476 even compared to open ocean pelagic fluxes. For example, open-ocean pelagic fluxes of up to
477 0.66 mg/cm²/yr have been reported in the central equatorial Pacific at 9°N by Hernes et al.
478 (2001).

479

480 Of primary importance in interpreting the variation of mass fluxes determined using
481 sediment traps, are (i) source effects (e.g. variation of upper ocean productivity and particle
482 export); (ii) hydrodynamic factors (i.e. biases in collecting sinking materials from overlying
483 seawater as a result of turbulent bottom water current). It has been demonstrated previously
484 that both distance from the vent source and bottom water currents affected by rough seafloor
485 topography can be important drivers of temporal and spatial variability in hydrothermal mass
486 fluxes (German et al., 2002; Adams et al., 2011). Hydrodynamic effects may also affect time-
487 series records of mass flux over short periods (weeks to months) by changing sinking particle

488 velocities as well as modifying the effective surface area of the sediment trap (Siegel and
489 Deuser, 1997; Buesseler et al., 2007). Previous studies at the EPR 9-10°N area also
490 demonstrated an unexpected influence of surface-generated mesoscale eddies in the transport
491 of hydrothermal plume materials away from the ridge axis (Adams et al., 2011).

492

493 Hence, the relatively large range in mass fluxes recorded in traps R1 and R2 through
494 time (**Table 2**) is more likely to be due to hydrodynamic transport variations rather than any
495 changes in the gross hydrothermal fluxes emitted from the vent site. Because the “RESET”
496 traps near Tica and Bio9 lacked precise navigation and were positioned out of the trough
497 (Mullineaux et al., 2010), their mass fluxes cannot be compared to other sediment traps
498 deployed at mid-ocean ridges that show strong relationships with distance from their vent
499 sources (German et al., 2002). Because trap R2 records the lowest mass flux, it could be
500 suggested that this trap represents non-hydrothermal background fluxes in the area. The
501 fluxes of Fe, Al, Cu, Zn, P, V for R2 trap (25 $\mu\text{g Fe/cm}^2/\text{yr}$, 11 $\mu\text{g Al/cm}^2/\text{yr}$, 0.8 $\mu\text{g Cu}$
502 cm^2/yr , 0.62 $\mu\text{g Zn/cm}^2/\text{yr}$, 2.7 $\mu\text{g P cm}^2/\text{yr}$, 0.04 $\mu\text{g V cm}^2/\text{yr}$ **Table 3**) are indeed similar to
503 previously reported background data for the deep Pacific Ocean above the East Pacific Rise
504 (Cowen et al., 2001) and Juan de Fuca Ridge (Dymond and Roth, 1988; German et al., 2002)
505 as well as pelagic to mesopelagic open ocean data (Jickells et al., 1984; Lamborg et al., 2008).
506 The flux of Mn in Trap R2, however, is one order of magnitude higher than typical
507 "background" sediment (1.5 $\mu\text{g Mn/cm}^2/\text{yr}$), and is nearly identical to the Mn flux measured
508 in trap R1. The fluxes of CaCO_3 are identical between traps R1 and R2, suggesting that both
509 traps receive the same contribution of biogenic materials (organic carbon content was not
510 measured in trap R2, **Table 3**). Significant hydrothermal input is recorded in trap R1, as
511 shown by the relatively high fluxes of elements that are typically enriched in hydrothermal
512 sulfides Fe, Cu and Zn (**Table 3**). Increased fluxes of Al, P and V are also observed in trap
513 R1, suggesting higher contribution of Fe-oxyhydroxides, organic matter and Al-bearing
514 detrital or lithogenic materials entrained in plume environments. Overall, although elemental
515 fluxes measured in trap R1 are consistent with the record of a far-field plume (German et al.,
516 2002), the close location of the traps relative to Bio 9 suggest that the trap was not placed
517 directly downstream of any plume dispersion, yet still collected a significant input of
518 hydrothermal materials.

519

520 **3.3. Iron mineralogy in plume particles**

521 The mineralogy and Fe speciation of hydrothermal plume particles from the 'Tica' and
522 "R2" sediment traps have been investigated previously using synchrotron-based X-ray
523 absorption near edge structure (XANES) spectroscopy (Toner et al., 2009; Toner et al., 2012).
524 Those data, combined with XAS analyses of trap R1 and Bio9 samples indicated the presence
525 of Fe-oxyhydroxide minerals and a variety of sulfide minerals as well detrital materials (glass
526 and clay) and organic-rich aggregates (**Table 4**). Sulfide-associated iron accounts for ~ 90
527 mol % of the total iron present in trap R1 (e.g. R1-16) while it is only present as a minor
528 proportion in trap R2 (e.g. R2-5,7,10). In contrast, oxidized Fe(III) shows the opposite
529 pattern, with a number of trap samples (e.g. R1-16, Bio9-19, Tica-19) having nearly
530 undetectable amounts of Fe(III) oxyhydroxides. Nonsulfide Fe(II), glasses and silicates
531 (including Fe(III)-phyllosilicate) form the remaining 6–51 mol % of total Fe. The observed
532 occurrence of Fe sulfide and Fe(III) oxyhydroxides are consistent with previous predictions
533 and observations for plumes in general, and are in complete agreement with Fe XANES
534 results for the Tica non-buoyant plume (Breier et al. 2012). The relatively high proportion of
535 detrital materials detected in our sediment traps was not present in the near-field non-buoyant
536 plume, indicating that these components were derived from seafloor materials (e.g. volcanic
537 glass, sediments) and/or sinking particles.

538 The XRF maps reported by Toner et al. (2009) also demonstrated that Fe was often
539 associated with other elements such as S, Ca, Zn, Cu, As and Se which is consistent with
540 XRD analyses showing the occurrence of pyrite (FeS₂), marcasite (FeS₂), sphalerite (ZnS), and
541 chalcopyrite (CuFeS₂). Basalt fragments, both glass and olivine, were also detected in the
542 plume particles via Fe XANES analysis, explaining the associated of Fe with Ca, Ti, V, and
543 Mn. Hence, X-ray spectroscopy suggest that Fe bearing particles fell into five basic
544 categories: (1) Fe sulfide minerals, predominantly pyrite, (2) Fe oxyhydroxide derived from
545 either weathered pyrite or direct oxidation of Fe²⁺ (3) basaltic materials such as silicates and
546 glass, (4) sedimentary materials including phyllosilicates, and (5) biological debris and
547 organics. Our analyses of major and trace element compositions are consistent with the
548 observed mineralogy as discussed below.
549

550 **3.4. Geochemical composition and phase associations**

551

552 3.4.1. *Organic matter.*

553 The proportion of particulate organic carbon (POC) ranges from 2 to 15 wt% in the
554 'Tica', 'Bio9' and R1 traps (< 1 mm fractions only), yielding relatively similar averages for all
555 the traps at 7.9, 7.6 and 6.5 wt% respectively (**Table 3**). This enrichment in POC for Trap R1
556 was previously discussed by Bennett et al. (2011b) but it remains unclear what the source of
557 this organic carbon might be. It is well recognized that chemoautotrophic production of
558 organic carbon in diffuse-flow hydrothermal environments has the potential to provide a
559 source of organic carbon to the deep-ocean that can be entrained into non-buoyant plumes
560 (German et al., 2015). We consider that the organic carbon content in our sediment traps,
561 therefore, may be derived from entrained organic carbon and microbial biomass from the base
562 of local buoyant hydrothermal plumes in addition to *in situ* production within the non-buoyant
563 plume.

564

565 3.4.2. *Carbonate component.*

566 The proportion of inorganic carbon (PIC) ranges from 0.8 to 6 wt% in the 'Tica' and
567 'Bio9' traps and from 0.2 to 2 wt% in the R1 trap. Determined as the carbonate component,
568 this suggests that carbonate (CaCO_3) represents on average about 20 wt% of the recovered
569 plume materials in 'Tica' and 'Bio9', and 8 wt% for R1 trap. The strong correlation between
570 PIC and Ca concentrations (**Figure 2a**) with a molar ratio PIC/Ca close to unity confirms the
571 presence of biogenic carbonate in the sediment trap. Because Ca, and other carbonate-
572 associated elements such as Sr, may be also associated with volcanic materials (glass
573 fragment and minerals), we compared Ca/Al and Sr/Al ratios (**Figure 2b**). Results show a
574 strong correlation between Ca/Al and Sr/Al yielding a Sr/Ca ratio of about 1.60 ± 0.12 (2se)
575 mmol/mol for < 1 mm particles in all sediment traps. This ratio is consistent with biogenic
576 carbonate, albeit with a slightly higher ratio than the Sr/Ca value of 1.4 - 1.5 mmol/mol
577 measured in planktonic foraminifera (Brown and Elderfield, 1996). Enrichment of Sr versus
578 Ca is clearly more pronounced in trap R1 for the > 1 mm particles (Sr/Ca of about 4
579 mmol/mol) suggesting the occurrence of aragonite in this sediment trap. These results are
580 consistent with previous sediment trap studies showing that aragonite can account up to 50%
581 of total calcium carbonate fluxes (Berner and Honjo, 1981).

582

583 3.4.3. *Volcanic material.*

584 The presence of volcanic material in our traps is well illustrated by the strong
585 correlation between Al and Ti in the plume particles, regardless of size fraction or the location

586 of the sediment traps relative to vent sources (**Figure 2c**). The overall Ti/Al ratio is about
587 0.097 ± 0.008 (2se, g/g) which is indistinguishable from the average Ti/Al ratio of $0.106 \pm$
588 0.006 (2sd, g/g) determined in lavas formed from the 2005-2006 eruption at EPR 9°50'N
589 (Goss et al., 2010). Further examination of Si versus Al relationships (**Figure 2d**) reveals the
590 predominance of 2 distinct geochemical groups: (i) the R1 trap exhibits the highest
591 hydrothermal contribution with Si/Al ≈ 2.64 ; (ii) other traps (Tica, Bio9 and R2) reflect
592 predominantly background sedimentation with higher Si/Al ratios >7.0 . Since the average
593 Si/Al of volcanic glass at EPR 9°50'N is 2.95 ± 0.04 (2sd, g/g), we consider that the
594 enrichment in Si versus Al in the background sediment traps is due primarily to the addition
595 of biogenic silica from phytoplankton debris, although some addition of terrigenous clay
596 material with Si/Al ≈ 4.4 (Plank and Langmuir, 1998) may also occur. The apparent scatter in
597 the Mg versus Al relationship (**Figure 2e**) is best explained by the fact that Mg is hosted in
598 several mineral phases, including olivine and carbonate. Nevertheless, the overall Mg/Al ratio
599 of 0.62 ± 0.18 is consistent with a major control of Mg and Al by volcanic glass with Mg/Al =
600 0.617 ± 0.012 (2sd, g/g). Hence, the composition of sinking plume materials is strongly
601 affected by the contribution of volcanic debris originating from recent lava flows in the axial
602 summit trough. Because all traps show the overall same extent of volcanic material input, we
603 posit that such materials are not only entrained in the ascending buoyant plume but also occur
604 as suspended background particles in the water column. Presumably, the recent volcanic
605 eruption that occurred less than a year before the sampling date provided an effective means
606 for exposing fresh volcanic material at the seafloor that could be resuspended into the deep
607 water column directly above the ridge axis.

608

609 *3.4.4. Metalliferous sediments and detrital materials.*

610 The relatively large Mn enrichment in the Tica, Bio9 and R2 sediment trap samples
611 relative to R1 and in previous studies from EPR 13°N is intriguing (**Table 3**). Micro-XRD for
612 the non-buoyant EPR plume showed a range of mineral phases hosting Mn, including MnS
613 (rambergite & alabandite), MnS₂ (hauerite), CuMnO₂ (crednerite), Mn₂O₃ (bixbyite) (Breier
614 et al., 2012). Determining the exact nature and source of mineral phases hosting Mn in our
615 trap samples is complex since Mn may occur as (i) Mn oxyhydroxide phases freshly formed
616 during aging and dispersing of the hydrothermal plume; (ii) Mn-rich sedimentary materials
617 entrained in the buoyant plume rising above hydrothermal vent sites; and (iii) Mn from
618 volcanic materials. Due to its very low oxidation kinetics (Cowen et al., 1986) Mn, in contrast
619 to Fe, remains predominantly in solution in hydrothermal plumes, at least over short distances

620 and timescales. Hence, trap R1 received the highest concentration of hydrothermal materials
621 and, closest to the vent source, should have received proportionally less Mn input than other
622 traps. As shown in **Table 3**, all traps (i.e. < 1mm particles) received relatively similar Mn
623 fluxes between 1.3 and 1.7 $\mu\text{g}/\text{cm}^2/\text{yr}$ regardless of their Fe fluxes, suggesting very limited
624 contributions of 'freshly formed' plume-derived Mn oxyhydroxides. The examination of Mn
625 versus Al relationships reveals two distinct geochemical groupings (**Figure 2f**). On one hand,
626 the R1 trap displays an enrichment in Mn and Al that is broadly consistent with the addition
627 of volcanic material with $\text{Mn}/\text{Al} = 0.018 \pm 0.002$ (2sd, g/g) (Goss et al., 2010). On the other
628 hand, background traps R2, Tica and Bio 9 show a much larger enrichment in Mn ($\text{Mn}/\text{Al} \approx$
629 0.5 g/g) well above crustal values and more consistent with the addition of authigenic Mn. As
630 shown in **Figure 3a**, Ba is also enriched in particles from these background traps, yielding
631 $\text{Ba}/\text{Mn} \approx 0.5 \text{ g/g}$ for the R2 trap and 0.3 g/g for the Tica and Bio9 traps. Ba enrichment in
632 settling particles and deep-sea sediments has been commonly associated with organic
633 productivity (Dymond et al., 1992). Ba/POC ratios in marine sinking particles generally show
634 an increase with depth, yielding Ba/POC ratios of about 0.02 to 0.04 (g/g) in deep water
635 which is higher than the ratios measured in the plume particles we have collected at EPR
636 $9^\circ 50' \text{N}$ where Ba/POC ratios are $\sim 0.01 \text{ (g/g)}$ (**Figure 3b**). Considering that Ba is barely
637 scavenged by Mn oxyhydroxide phases in hydrothermal plumes (Feely et al., 1996), we favor
638 a secondary origin for both Mn and Ba in our sediments traps including the resuspension of
639 metalliferous sediments. This hypothesis is consistent with previous work showing that Ba
640 may be associated with amorphous Mn oxides in hydrothermal sediments on ridge flanks
641 (Ruhlin and Owen, 1986; Cronan and Hodkinson, 1997) and that bottom sediment
642 resuspension is the dominant factor controlling the increase of benthic particulate Mn and Ba
643 in seawater (Feely et al., 1994).

644

645 *3.4.5. Iron oxyhydroxide component.*

646 It has been well established that Fe oxyhydroxides provide an effective means to
647 scavenge dissolved seawater oxyanions such as P, V, As and Cr (Trocine and Trefry, 1988;
648 Feely et al., 1990; Feely et al., 1991; German et al., 1991b) leading to constant molar ratios of
649 P/Fe and V/Fe dependent on the local dissolved phosphate concentration (Feely et al., 1998).
650 Strong correlations between particulate Fe, P, V, Cr and As concentrations have been
651 particularly well described in the hydrothermal plume at EPR $9^\circ 50' \text{N}$ (Feely et al., 1994;
652 Breier et al., 2012). In theory, it is possible to calculate the relative abundance of
653 hydrothermally-sourced Fe-oxyhydroxide materials in bulk sediment trap particles, using V

654 and P versus Fe relationships. This approach, which has been used in several studies of
655 sediment trap and suspended plume particles (German et al., 2002; Bennett et al., 2009),
656 exploits the scavenging properties of Fe oxyhydroxides for P and V oxyanions in seawater.
657 By knowing the V/Fe and P/Fe ratios in the pure hydrothermal Fe-oxyhydroxide pool, it is
658 possible to determine the proportion of this pool in bulk sample. An important caveat
659 however, is that this approach assumes that all the measured P and V in the sediment traps is
660 associated with Fe-oxyhydroxides. Since V and P are also found in association with volcanic
661 materials and/or biogenic compounds in the sediment traps at EPR 9°50' N, we critically
662 evaluate the phase association of P and V in our samples, below.

663

664 As shown in **Figure 3c**, V/Fe ratios in all plume fall-out materials correlate with
665 Al/Fe, defining two groups: Reset traps (Bio9 and Tica) with an overall V/Al \approx 0.003 and R1-
666 R2 traps with V/Al \approx 0.018, which is identical, within uncertainty, to the V/Al ratio measured
667 in volcanic glass at EPR 9°50'N (V/Al = 0.0019) by Goss et al. (2010). In addition, V/Fe
668 ratios for background traps 'Tica' and 'Bio9' yield higher values than those obtained
669 previously for suspended non-buoyant plume particles at EPR 9°50'N (V/Fe \approx 0.002) by
670 Breier et al. (2012) and V/Fe \approx 0.0038 (mol/mol) by Feely et al. (1994). Hence, to a first
671 approximation, most of the variations in V/Fe ratios observed in plume particles collected in
672 the aftermath of the 2005/06 eruption resulted primarily from the addition of volcanic
673 materials. In detail, a close examination of V/Fe and Al/Fe relationships for trap R1, which
674 received the largest hydrothermal input (**Figure 3d**), suggests that non-volcanic components
675 in the plume material have V/Fe \approx 0.0001 (i.e. intercept at Al/Fe=0, Figure 3d). This suggests
676 that, as a whole, Fe-oxyhydroxides contribute far less than 5% of the hydrothermally-derived
677 Fe. Note that the determination of the proportion of Fe-oxyhydroxides using mass balance
678 consideration may differ from spatially-resolved Fe XANES analysis (Table 4) considering
679 the heterogeneous nature of the sediment trap materials.

680 Another means for determining Fe-oxyhydroxide proportions is the use of P/Fe. In
681 previous studies, P/Fe ratios of suspended particles from the non-buoyant plume at EPR
682 9°50'N were determined to be 0.06 (Breier et al., 2012) and 0.18 (Feely et al., 1994), with
683 differences potentially related to particle ages (Breier et al., 2012). Excluding the background
684 sediment trap R2, we obtained P/Fe values up to 0.30 (mol/mol) in trap R1 and up to 0.10
685 (mol/mol) for the Tica and Bio9 traps (**Figure 3e,f**). Because POC concentrations were only
686 measured on the < 1 mm fractions from the R1, Tica and Bio9 traps, it is not possible to
687 compare POC and P enrichments for all fractions of the sediment trap samples. However, as

688 presented in **Figure 3e** a correlation is observed between POC/Fe and P/Fe ($r^2=0.8$) defining
689 a relationship characterized by $P/POC \approx 0.0056$ and initial $P/Fe \approx 0.01$ (i.e. calculated at
690 $POC/Fe = 0$). This suggests an overall C/P of about 180 (mol/mol), which is higher than the
691 classical Redfield ratio of 106 and is the highest range for marine phytoplankton anywhere in
692 the Pacific Ocean (Sterner et al., 2008). Similarly, N/P ratios at EPR 9°50'N (Table 2) have
693 been also determined at about 26 mol/mol which is higher than the Redfield ratio of 16-19
694 (Sterner et al., 2008). Hence, although organic matter in the sediment traps appears relatively
695 depleted in P, it provides the main host for P, with only a small proportion (i.e. less than 5%
696 based on initial $P/Fe \approx 0.01$) that could be attributed to PO_4 adsorption onto Fe-
697 oxyhydroxides. This result is consistent with the V/Fe ratios discussed above. Observing a
698 non-Redfield ratio for the organic matter recovered in sediment traps is not unexpected
699 considering the fundamentally different source and nature of organic compounds in seafloor
700 hydrothermal plumes (Toner et al., 2009). This also confirms that phytoplankton debris
701 cannot contribute significantly to the overall organic carbon enrichment found in
702 hydrothermal plumes as discussed previously (Bennett et al., 2011b).

703

704 3.4.6. Iron sulfide material.

705 The enrichment of sulfide materials in plume particles is often associated with an
706 increase in chalcophile element concentrations such as Cu and Zn (Trocine and Trefry, 1988;
707 Mottl and McConachy, 1990; German et al., 1991a). The main chimney-forming sulfide
708 minerals reported from the Bio9 and Tica vents include primarily chalcopyrite ($CuFeS_2$),
709 pyrite and marcasite (FeS_2), and sphalerite (ZnS) (Rouxel et al., 2008a). Because Fe is also
710 hosted in detrital and volcanic materials, we have normalized sulfide-associated elements to
711 Al. The variations of Cu/Al, Co/Al and Zn/Al all show strong correlations with Fe/Al
712 (**Figure 4 a-c**) with $r^2 \approx 0.8$ over the entire data set confirming that, besides volcanic
713 materials, Fe is primarily present in the form of polymetallic sulfide minerals. The normative
714 mineralogy of these sulfides cannot be determined directly, however, due to the absence of
715 sulfur concentration data arising from the use of DMSO as the sample preservative in the
716 sediment trap cups. Nevertheless, the molar ratios of Cu/Fe and Zn/Fe of 0.04 and 0.023
717 respectively do suggest a predominance of Fe-sulfides (pyrite, marcasite and/or pyrrhotite)
718 over other sulfide minerals such as chalcopyrite and sphalerite, which contrasts with the
719 observed mineralogy of hydrothermal chimneys at the Bio9 site where chalcopyrite represent
720 a major mineral (Rouxel et al., 2008a). The Cu/Fe and Zn/Fe ratios of the plume materials
721 reported here, however, are consistent with the end-member fluid values measured at Bio9

722 (Cu/Fe \approx 0.016 to 0.06 and Zn/Fe \approx 0.016 to 0.06 ratios at Bio9, Table 1). This is consistent
723 with the hypothesis that the sulfides recovered in the traps represent primary plume minerals,
724 formed in situ in the buoyant plume, rather than chimney materials entrained in the ascending
725 fluids.

726 *3.4. Fe isotope composition of sediment traps*

727 Fe isotope compositions of plume particles are presented in **Table 2**. Trap R1,
728 receiving the greatest input of hydrothermal materials yields a relatively restricted range of
729 $\delta^{56}\text{Fe}$ values between -0.84 and -0.40‰, with an average of -0.63 ± 0.04 ‰ (2se, n=42).
730 These values are systematically lighter than the end-member vent-fluid $\delta^{56}\text{Fe}$ values of $-0.41 \pm$
731 0.04 ‰ (2sd, n=4) measured at Bio9 after and before the 2006/2007 eruption. The
732 background traps 'Tica' and 'Bio9' yield similar average $\delta^{56}\text{Fe}$ values at -0.55 ± 0.13 ‰ (2se,
733 n=6) with an overall range of -0.30 to -0.78‰. In comparison, the other background trap R2
734 yields the largest range of $\delta^{56}\text{Fe}$ values from -0.91 to -0.03‰. These values span those of
735 igneous $\delta^{56}\text{Fe}$ values at $\approx +0.09$ ‰ and isotopically light sulfides measured in the Bio9
736 chimney, in particular pyrite/marcasite assemblages with $\delta^{56}\text{Fe}$ values as low as -1.26 ‰
737 (Rouxel et al., 2008a). In trap R1, the fine < 1 mm fraction displays the same average $\delta^{56}\text{Fe}$
738 value as the coarse > 1 mm fraction ($\delta^{56}\text{Fe} = -0.62 \pm 0.05$ ‰ vs. -0.64 ± 0.06 ‰ (2se, n=42))
739 suggesting a homogeneous distribution of Fe isotopes among both particle pools.

740
741 Previous experimental investigations have highlighted the importance of Fe redox
742 cycling, mineral precipitation and dissolution as factors contributing to Fe isotope
743 fractionation. In plume environments, Fe isotopes can be fractionated by abiotic and/or biotic
744 Fe(II) oxidation and precipitation of ferric hydroxides (Bullen et al., 2001; Balci et al., 2006;
745 Wu et al., 2010; Wu et al., 2011b) and Fe-sulfide precipitation (Butler et al., 2005; Guilbaud
746 et al., 2011; Wu et al., 2012). Fe-rich particles in buoyant and non-buoyant plume samples
747 from the Rainbow vent-field (Mid-Atlantic Ridge) have been investigated previously and
748 yielded heavier $\delta^{56}\text{Fe}$ values from 0.1 to 1.1‰ relative to their source vent-fluid (Severmann
749 et al., 2004), consistent with isotopic fractionation during partial oxidation of Fe(II)aq to
750 Fe(III)aq in plume environments. In another study at 5°S, Mid-Atlantic Ridge (MAR),
751 Bennett et al. (2009) investigated the Fe isotope systematics of both end-member vent fluids,
752 and the rising buoyant plume particles collected directly above the same vents. They
753 demonstrated that the isotope fractionation caused by the formation of Fe-sulfides in plume

754 environments favor an enrichment in light Fe isotopes in Fe-sulfides, with an overall
755 fractionation factor of $+0.60 \pm 0.12\%$. More recently, Revels et al. (2015) showed that both
756 total-digestible and labile Fe within a hydrothermal plume sampled at the TAG hydrothermal
757 field on MAR are characterized by heavier $\delta^{56}\text{Fe}$ relative to the vent source. Decreasing Fe
758 concentration and $\delta^{56}\text{Fe}$ with distance from the vent are consistent with the water-column
759 precipitation of Fe-oxyhydroxides within the buoyant plume. Hence, the precipitation of Fe-
760 oxyhydroxides or Fe-sulfides have opposite effects on the Fe isotope composition of plume
761 particles.

762 Because volcanic materials are also an important component of the plume materials
763 recovered by our sediment traps, the Fe isotope composition of the plume particles should
764 represent mixing of at least 3 components: (1) sulfides with $\delta^{56}\text{Fe}$ values lower than source
765 vent-fluids, (2) Fe-oxyhydroxides with $\delta^{56}\text{Fe}$ values higher than source vent-fluids and (3)
766 volcanic materials with $\delta^{56}\text{Fe}$ values near crustal values. Considering that Al/Fe ratios are
767 good proxies for the relative proportion of volcanic versus hydrothermal materials in plume
768 fall-out particles, we compared $\delta^{56}\text{Fe}$ versus Al/Fe in **Figure 4d**. Results show that $\delta^{56}\text{Fe}$ are
769 globally consistent with the mixing of isotopically light hydrothermal end-members (Al/Fe =
770 0) and volcanic materials characterized with $\delta^{56}\text{Fe} = 0.09\%$ (Beard et al., 2003a; Rouxel et
771 al., 2003; Teng et al., 2013) and Al/Fe = 2.2 mol/mol (Goss et al., 2010). The correlation,
772 however, is relatively weak ($r^2 = 0.56$). This suggests significant variations in $\delta^{56}\text{Fe}$ values of
773 the hydrothermal components, probably in the range of -0.2 down to -1.2 ‰ in order to
774 explain the entire variation of $\delta^{56}\text{Fe}$ versus Al/Fe values (**Figure 4d**). While the heaviest and
775 lightest values are consistent with precipitation of Fe-oxyhydroxides and Fe-sulfides
776 respectively, the isotopic signature of each component requires a careful examination of their
777 relative proportions, as discussed in the following section.

778

779 **4. Geochemical model**

780 *4.1. Determination of mixing components*

781 The examination of the mineralogy and elemental composition of our plume particles
782 has suggested seven major components: (1) Fe-sulfide precipitates (pyrite/marcasite,
783 pyrrhotite, chalcopyrite, sphalerite) enriched in Cu, Co, and Zn; (2) volcanic materials defined
784 by their strong correlation between Al and Ti (e.g. volcanic glass from recent volcanic
785 eruption) (3) Fe-oxyhydroxides formed through partial oxidation of Fe(II), scavenging P and

786 V; (4) metalliferous sediment enriched in Mn and Ba remobilized from seafloor
 787 environments; (5) biogenic carbonate controlling Ca and Sr enrichment; (6) biogenic silica
 788 from phytoplankton debris yielding an excess Si enrichment; (7) organic matter-rich
 789 materials, derived both from sinking planktonic debris and from new production associated
 790 with seafloor venting.

791 To define further the fluxes of the different components, a normative analysis
 792 approach, which quantitatively partitions the trap compositions into the seven components
 793 listed above, was carried out. The analysis uses linear programming to determine the mixture
 794 of these components which best accounts for the observed Al, Si, Ca, Sr, Fe, Mn, P, V, Cu
 795 and Zn contents of the trap samples. The results have been also used to assess the relative
 796 contributions of the different Fe pools in the plume particles and their Fe-isotope
 797 composition. The geochemical compositions of the different components are listed in **Table 5**
 798 together with their uncertainty. End-member values for Fe-oxyhydroxides, metalliferous
 799 sediments and volcanic materials have been derived from previously published values (Feely
 800 et al., 1994; Goss et al., 2010; Mills et al., 2010; Breier et al., 2012) while carbonate and
 801 organic matter values were determined from the relationships between TOC versus P and TIC
 802 versus Ca and Sr.

803 Considering a total number of plume components of 7, a minimum of 7 equations
 804 defined by the mass conservation relationships of 7 elements is required to determine each
 805 component. Since our geochemical composition dataset contains a larger number of elements,
 806 the system is typically over-constrained. Here, we use the concentrations of 10 elements Al,
 807 Si, Ca, Sr, Fe, Mn, P, V, (Cu+Zn) (**Table 5**) which optimally describe the main geochemical
 808 variations of the system. The approach used to determine the amount of each component is
 809 similar to the determination of normative mineralogy as described in several models (Banks,
 810 1979; Cohen and Ward, 1991; Pruseth, 2009). Independent knowledge about the abundance
 811 of several of the minerals in the sample can be done through solving a set of linear equations.
 812 We first consider species i held in phase j . M_j is the mass (or mass flux) of phase 'j' and m_j^i the
 813 mass of species i contained in phase j . Mass conservation requires:

$$814 \quad M_o = \sum_{j=1}^n M_j \quad (2)$$

815 The sum of all the phases for element i is defined by

$$816 \quad m_o^i = \sum_{j=1}^n m_j^i \quad (3)$$

817 The concentration of species i in phase j is thus defined as $C_j^i = m_j^i / M_j$. Table 4 therefore
818 represents the matrix composition of C_j^i values.

819

820 For the determination of each M_j values, we implement a simple calculation scheme using
821 Microsoft Excel spreadsheet formulas and matrix solving, such as:

$$822 \quad M_j = C_j^{i^{-1}} * m_j^i \quad (4)$$

823 We also applied a stochastic error propagation scheme using a Monte Carlo simulation.

824

825 Because the chemical composition of each component is relatively simple (**Table 5**),
826 the calculation scheme was done by establishing priority among minerals while preventing
827 negative input data generation. The results of the average mass fluxes for each component are
828 presented in **Table 6** and individual data are presented in **Figures 5 & 6**.

829

830 Next, we calculated the contribution of each component to the total Fe inventory and
831 established an Fe isotope mass balance according to the equation.

832

$$833 \quad \delta^{56}\text{Fe}_{\text{bulk}} = X_{\text{Fe}_{\text{FeOOH}}} \delta^{56}\text{Fe}_{\text{FeOOH}} + X_{\text{Fe}_{\text{FeS}_2}} \delta^{56}\text{Fe}_{\text{FeS}_2} + X_{\text{Fe}_{\text{Volc}}} \delta^{56}\text{Fe}_{\text{Volc}} + X_{\text{Fe}_{\text{Sed}}} \delta^{56}\text{Fe}_{\text{Sed}}$$

834 Because the Fe isotope compositions of metalliferous sediments ($\delta^{56}\text{Fe}_{\text{Sed}}$), sulfides
835 ($\delta^{56}\text{Fe}_{\text{FeS}_2}$) and Fe oxyhydroxides ($\delta^{56}\text{Fe}_{\text{FeOOH}}$) are all unknown, we grouped them together as
836 $\delta^{56}\text{Fe}_{\text{HYD+SED}}$. The proportion of Fe distributed among different components ($X_{\text{Fe}_{\text{FeOOH}}}$,
837 $X_{\text{Fe}_{\text{FeS}_2}}$, $X_{\text{Fe}_{\text{Volc}}}$, $X_{\text{Fe}_{\text{Sed}}}$) was determined using results the results generated for the
838 determination of mass fluxes. We determined $\delta^{56}\text{Fe}_{\text{HYD+SED}}$ values by assuming $\delta^{56}\text{Fe}_{\text{Volc}} =$
839 0.09‰. Results are presented in **Table 6** and **Figures 7 & 8**. We also applied an error
840 propagation scheme for the determination of all results presented.

841

842 **4.2. Dynamics of plume components**

843 The temporal variations of calculated mass fluxes for each plume component in trap
844 R1 show pulses at the beginning and end of the deployment (i.e. at 40 and 160 days elapsed
845 since May 16th 2006) and also at 90 and 120 days (**Figure 5**). This 30-40 day periodicity in
846 mass flux is seen for both particle size fractions (i.e. < 1 mm and > 1 mm) and is directly
847 related to pulses in both hydrothermal (i.e. Fe sulfides) and volcanic material deposition
848 (**Figure 5**). The co-variation between hydrothermal and volcanic fluxes suggests common

849 sources, probably from the entrainment of seafloor volcanic materials in the buoyant part of
850 the plume in chimney environments. The R1 sediment trap is located 25 m away from Bio9
851 and therefore underlies the buoyant plume. Although changes in primary vent output cannot
852 be ruled out, analyses of changes in current flow at this site are sufficient to explain the
853 observed temporal variability in mass fluxes for both hydrothermal and volcanic materials. In
854 particular, subinertial variability of the near-bottom currents on time scales of 30-40 days was
855 previously reported on the EPR crest at 9°50'N (McGillicuddy et al., 2010; Liang and
856 Thurnherr, 2011; Liang and Thurnherr, 2012). Some of this variability may be related to
857 mesoscale eddies (Adams et al., 2011), as well as different flow regimes or turbulence levels
858 associated with different water masses on the ridge crest (Liang and Thurnherr, 2012).

859 In contrast, mass fluxes for metalliferous sediments, biogenic components and organic
860 materials seem unrelated to hydrothermal and volcanogenic fluxes (**Figure 6**). The increase of
861 organic matter flux from large particles observed within the first 30 days of trap deployment
862 (**Figure 6**) probably corresponds to an increase in larval supply. Both larval supply and mass
863 flux are derived from independent pools built up over time, so changes in production should
864 not be correlated with hydrothermal fluxes (Adams et al., 2011). Both biogenic and
865 metalliferous sediment fluxes show marked increases at the beginning and end of R1 trap
866 deployment, which might best be explained by the resuspension of thin Mn-coatings and
867 sediment dusting that covered ancient lava flows nearby (Templeton et al., 2005; Santelli et
868 al., 2008). This is similar to the “rebound” model used by Walsh et al. (1988) which assumes
869 that material settling to the seafloor is resuspended without particle sorting.

870

871 **4.3. Fe isotope systematics**

872 In order to discuss the processes affecting Fe isotope composition in plume particles, a
873 first priority is to demonstrate that Fe-isotope variability is not the result of mixing between
874 hydrothermal and lithogenic particles derived from the surrounding volcanic rocks. As shown
875 in **Table 6**, the average Fe isotope compositions of plume particles corrected for volcanic
876 components ($\delta^{56}\text{Fe}_{\text{HYD+SED}}$) range from $-0.86 \pm 0.12\text{‰}$ (1s, R2 trap < 1mm) to $-0.66 \pm 0.16\text{‰}$
877 (Bio9 trap). Trap R1 yields identical $\delta^{56}\text{Fe}_{\text{HYD+SED}}$ values for both size fractions with $-0.69 \pm$
878 0.11‰ and $-0.73 \pm 0.14\text{‰}$ for the < 1mm and > 1mm fractions, respectively. The Tica trap
879 also yields similar average values of $-0.72 \pm 0.15\text{‰}$. These values are systematically lighter
880 and more variable than the hydrothermal fluid end-member values at Bio9: $-0.41 \pm 0.02\text{‰}$

881 (Table 1). Only one $\delta^{56}\text{Fe}_{\text{HYD+SED}}$ value from the background R2 trap (> 1mm fraction) shows
 882 heavier values of $-0.14 \pm 0.28\%$. This trap also features the largest range of values, down to -
 883 $1.3 \pm 0.19\%$. Trap R2, as well as Tica and Bio9, exhibits the largest contribution from
 884 metalliferous sediments up to 60% with Fe-oxyhydroxide up to 25% relative to the total non-
 885 volcanic Fe pool (**Figure 8**). In particular, the largest variations in $\delta^{56}\text{Fe}_{\text{HYD+SED}}$ are observed
 886 for samples with significant contributions of sedimentary material enriched in Mn, suggesting
 887 the input of exotic and heterogeneous materials derived from surrounding environments.

888 In trap R1, $\delta^{56}\text{Fe}_{\text{Bulk}}$ values are clearly related to the relative mixing between volcanic
 889 materials and Fe-sulfides, with pulses of heavier values that mirror an increase in the
 890 proportion of volcanic materials (**Figure 7**), and a corresponding decrease in the proportion of
 891 Fe-sulfides. In contrast, no systematic co-variations of $\delta^{56}\text{Fe}_{\text{HYD+SED}}$ with the proportion of
 892 Fe-oxyhydroxide is observed, although lowest $\delta^{56}\text{Fe}_{\text{HYD+SED}}$ values at day 84 also correspond
 893 to the lowest proportion of Fe-oxyhydroxide present (**Figure 8**). This suggests that the overall
 894 negative Fe isotope composition in plume particles dominated by Fe-sulfides may be muted
 895 by the addition of small amounts of isotopically heavier Fe-oxyhydroxides, likely derived
 896 from the non-buoyant plume sample (Breier et al., 2012)

897

898 ***4.4. Implications for the marine iron isotope budget***

899 If no Fe is lost from (or gained by) the buoyant plume, the bulk Fe isotope
 900 composition of the plume should remain constant and should be similar to the initial
 901 composition of the hydrothermal fluids ($\delta^{56}\text{Fe}_{\text{HT}}$). This enables us to establish an iron isotope
 902 budget, such as:

$$903 \quad \delta^{56}\text{Fe}_{\text{Total}} = \delta^{56}\text{Fe}_{\text{HT}} = X_{\text{PFe}} * \delta^{56}\text{Fe}_{\text{PFe}} + (1 - X_{\text{PFe}}) * \delta^{56}\text{Fe}_{\text{DFe}} \quad (5)$$

904 with $\delta^{56}\text{Fe}_{\text{DFe}}$ the Fe isotope composition of dissolved Fe (DFe) and X_{PFe} the fraction of total
 905 Fe precipitated as Fe-sulfides. Although Fe-oxyhydroxides are potentially present in the plume
 906 particles, they represent only a small fraction of the total Fe in near-vent plume particles, as is
 907 especially the case for trap R1. Hence, X_{PFe} may be theoretically determined by knowing the
 908 Fe isotope fractionation factor ($\Delta\delta^{56}\text{Fe}_{\text{FeS-DFe}}$) between Fe-sulfide particles and dissolved Fe
 909 such as:

$$910 \quad X_{\text{PFe}} = 1 + (\delta^{56}\text{Fe}_{\text{HT}} - \delta^{56}\text{Fe}_{\text{PFe}}) / \Delta\delta^{56}\text{Fe}_{\text{FeS-DFe}} \quad (6)$$

911 Based on previous studies in the hydrothermal plume at MAR 5°S (Bennett et al.,
912 2009), the fractionation factor for Fe-sulfide precipitation has been calculated at $\Delta\delta^{56}\text{Fe}_{\text{FeS-DFe}}$
913 = $-0.60 \pm 0.12\text{‰}$. This is consistent with experimental studies by Butler et al. (2005), where a
914 kinetic isotope fractionation of up to $-0.85 \pm 0.30\text{‰}$ was observed for zero age Fe-sulfides
915 over a temperature range between 2 and 40°C. During aging, the degree of fractionation
916 during that study decreased to -0.3‰ between the precipitates and the fluid. In more recent
917 experimental studies (Guilbaud et al., 2011; Wu et al., 2012), the equilibrium fractionation
918 factor has been determined to range from $+0.32 \pm 0.29\text{‰}$ (2s) to $+0.64 \pm 0.36\text{‰}$ (2s) between
919 mackinawite (FeS_m) and $\text{Fe}^{2+}_{\text{aq}}$ (with minor FeS_{aq} also present in the experiment) at
920 temperature $< 25^\circ\text{C}$. This implies that depending on the degree of FeS_m precipitation from
921 solution, and the degree of isotope exchange during equilibration, $\Delta\delta^{56}\text{Fe}_{\text{FeS-DFe}}$ values may
922 display a 1.4‰ range, from positive values in the case of equilibrium processes to negative
923 values in the case of kinetic processes. Considering that the precipitation of Fe-sulfides
924 occurs rapidly in buoyant plumes as hydrothermal fluids mix with seawater, it is expected that
925 a significant kinetic Fe isotope effect will be observed. These results are also consistent with
926 previous studies by Rouxel et al. (2008) who reported light $\delta^{56}\text{Fe}$ values for suspended
927 particles from Ti end-member sample bottles (down to -1.8‰ , **Table 1**) which precipitated
928 upon sampling of high-temperature fluids at Tica vent.

929 Considering a range of $\Delta\delta^{56}\text{Fe}_{\text{FeS-DFe}}$ values between -0.6 to -1.2‰ , we obtain a range
930 of X_{PFe} between 0.5 to 0.8 suggesting that about 50 to 20% of the total Fe remained in
931 dissolved form in material toward the top of the buoyant plumes at the EPR 9°50'N site.
932 Considering a molar ratio of Fe/H₂S between 0.2 and 0.4 measured in the end-member vent
933 fluids at Bio9 (Von Damm, 2004; Yucel and Luther, 2013), dissolved Fe should
934 predominantly occur as soluble Fe-sulfides in the buoyant plume. Hence, it can be suggested
935 that our sediment traps preferentially collected coarse, rapidly-sinking pyrite and other Fe-rich
936 sulfide particles falling out in the near-field at EPR 9°50'N while the remaining Fe was
937 exported through the buoyant plume as finer-grained particles or aqueous Fe complexes.
938 Using our mass balance approach, we also determine that the Fe isotope composition of the
939 remaining dissolved or suspended Fe pool ($\delta^{56}\text{Fe}_{\text{DFe}}$) should range from -0.1 to $+0.5\text{‰}$, which
940 is significantly heavier than hydrothermal fluid values at -0.4‰ . As the majority of
941 hydrothermal venting, especially at fast spreading ridges, occurs in basalt-hosted systems, Fe
942 isotopes are expected to be fractionated due to Fe-sulfide precipitation in the buoyant plumes.
943 By non-buoyant plume height, a large amount of Fe-sulfide precipitates will have been lost

944 from the plume with a concomitant removal of isotopically light Fe. A similar model has been
945 also proposed to explain the relatively heavy Fe isotope signatures of the water column Fe
946 enrichment attributed to the EPR at 25°S; 105-90°W (Fitzsimmons et al., 2013). In this
947 previous study, $\delta^{56}\text{Fe}_{\text{DFe}}$ signatures were found to be relatively invariant at $+0.54 \pm 0.14\%$
948 ($n=9$) over two stations. Hence, from our study and others (Bennett et al., 2009; Fitzsimmons
949 et al., 2013), we can hypothesize that the Fe exported from hydrothermal vents should have an
950 isotopic signature heavier than the original vent fluid.

951 The isotopic composition of dissolved Fe in seawater has received great interest in
952 recent years (Lacan et al., 2008; John and Adkins, 2010; Lacan et al., 2010; Rouxel and Auro,
953 2010; Radic et al., 2011; Boyle et al., 2012; Conway and John, 2014). Radic et al. (2011)
954 reported Fe isotope values for open ocean seawater from the equatorial Pacific. Dissolved Fe
955 (DFe) concentrations ranged from 0.1 to 1.5 nM, yielding $\delta^{56}\text{Fe}$ values of $+0.01$ to $+0.58\%$
956 consistent with other Fe isotope results from the Southeastern Atlantic, with $\delta^{56}\text{Fe}_{\text{DFe}} = -0.14$
957 to $+0.23\%$ (Lacan et al., 2008) and from the North Atlantic near Bermuda with $\delta^{56}\text{Fe}_{\text{DFe}} =$
958 $+0.30$ to $+0.71\%$ (John and Adkins, 2010). Conway and John (2014) also reported a high-
959 resolution transect of $\delta^{56}\text{Fe}_{\text{DFe}}$ values along a section of the North Atlantic Ocean. That study
960 allowed a first-order assessment of the potential contribution of different Fe sources to the
961 ocean, such as Fe derived from dust dissolution ($\delta^{56}\text{Fe}_{\text{DFe}}$ as high as 0.68%), Fe released
962 through reductive and non-reductive sedimentary dissolution ($\delta^{56}\text{Fe}_{\text{DFe}}$ considered at -2.4 and
963 $+0.09\%$ respectively), and Fe from seafloor hydrothermal venting ($\delta^{56}\text{Fe}_{\text{DFe}}$ measured at $-$
964 1.35% in the hydrothermal plume). This mass balance approach, however, implied that the Fe
965 isotope signatures of the different Fe sources are well characterized and conservative during
966 oceanic mixing. Our results at EPR 9°50'N and at MAR 5°S (Bennett et al., 2009) suggest
967 that (1) the Fe isotope composition of high-temperature vent fluids from basalt-hosted settings
968 is unlikely to be as light as -1.35% since the global average of fluid values is $-0.43 \pm 0.16\%$
969 (1SD; $n=39$), including our data and those reported elsewhere (Sharma et al., 2001; Beard et
970 al., 2003b); (2) the Fe isotope composition of a distal, non-buoyant hydrothermal plume is
971 expected to be shifted toward isotopically heavy values, *i.e.* in the opposite direction from far-
972 field $\delta^{56}\text{Fe}_{\text{DFe}}$ values, unless Fe-oxyhydroxide precipitation in the plume is dominating over
973 Fe-sulfide precipitation as found in a number of slow-spreading ridge settings (Severmann et
974 al., 2004; Revels et al., 2015). As discussed by Saito et al. (2013), measurements of dissolved
975 Fe to hydrothermal helium ratios in the far-field plume along the Mid-Atlantic Ridge suggest
976 proportionally higher iron fluxes from slow-spreading ridges, probably due both to the higher

977 concentration of focused vs diffuse axial heat flow along slow versus fast ridges (German et
978 al., 2016). In particular, both the fluxes of high temperature fluids and their Fe concentrations
979 are particularly pronounced in vent sites from slow spreading ridge and frequently ultramafic-
980 influenced settings. In those cases, where hydrothermal plumes exhibit unusually high
981 Fe/H₂S ratios (German et al., 2010) we should expect the generation of isotopically lighter
982 values for dissolved Fe in distal plumes due to the precipitation of isotopically heavy Fe-
983 oxyhydroxide particles before non-buoyant plume height is reached, just as has previously
984 been reported for the Rainbow hydrothermal field (Severmann et al., 2004) and observed in
985 dissolved $\delta^{56}\text{Fe}$ data from a plume at the TAG site in the North Atlantic (Conway and John,
986 2014). The same has also been seen in low-temperature hydrothermal deposits at the seafloor
987 (Rouxel et al., 2003). Hence, depending upon the geological setting, the Fe isotope
988 composition of far-field hydrothermal sources to the deep ocean could be expected to exhibit
989 $\delta^{56}\text{Fe}$ values that are either heavier or lighter than their source high-temperature vent fluids.
990 Additional studies bridging near-field and oceanic transects will be required, in future, to
991 investigate these processes further.

992

993 **5. Conclusion**

994 Considering the growing evidence for the far-field export of hydrothermally-sourced
995 Fe to the deep ocean (Bennett et al., 2008; Toner et al., 2009; Yucel et al., 2011; Carazzo et
996 al., 2013; Saito et al., 2013; Fitzsimmons et al., 2014), Fe isotopes should provide a means to
997 quantify such hydrothermal contributions to the global ocean. At EPR 9-10°N, we have
998 demonstrated that Fe isotope fractionation in the buoyant hydrothermal plume occurs during
999 the formation of Fe-sulfide precipitates. Their calculated $\delta^{56}\text{Fe}$ values range from $-0.73 \pm$
1000 0.13% to $-0.86 \pm 0.13\%$, *i.e.* systematically lower than their source hydrothermal vent-fluids
1001 ($\delta^{56}\text{Fe} = -0.4\%$). These results contrast directly with previous work at the ultramafic-
1002 influenced and sulfide poor Rainbow vent field on the MAR, where the Fe isotope
1003 composition of hydrothermal sediments beneath the plume were found to be indistinguishable
1004 from the vent fluid, and where Fe particles within the buoyant and non-buoyant plume
1005 exhibited values from 0.1 to 1.1% relative to the vent fluid, consistent with partial oxidation
1006 of Fe(II) to Fe(III). To date, however, the majority of hydrothermal venting that has been
1007 located occurs along fast-spreading ridges in the Pacific Ocean where vents are almost
1008 exclusively found in basalt-hosted settings (Beaulieu et al., 2016). In such situations, we

1009 predict that Fe isotopes should be fractionated to varying degrees during buoyant-plume Fe
1010 sulfide precipitation. By non-buoyant plume height, significant amounts of Fe-rich sulfides
1011 should be expected to have precipitated out of those plumes, and settled rapidly back toward
1012 the underlying seafloor causing a net removal of isotopically light Fe. Hence, it can be
1013 hypothesized that the stabilized dissolved Fe fraction that is exported to the deep ocean via
1014 non-buoyant hydrothermal plumes should have an Fe isotope signature that is heavier than its
1015 original vent fluid. This suggests that both the initial Fe isotope composition of any high-
1016 temperature vent fluids and the Fe/H₂S ratio of that source should combine to impose
1017 characteristic Fe isotope “fingerprints” for hydrothermally sourced Fe exported to the deep
1018 ocean. Using a time series approach, we have also demonstrated that the Fe isotope
1019 composition for high-temperature vent fluids is rather constant, even in response to an
1020 episode of seafloor eruptive volcanism, and that variations in the $\delta^{56}\text{Fe}$ values for rapidly
1021 sinking near-vent plume particles can most readily be explained by local processes leading to
1022 variable mixing of hydrothermal, biogenic and lithogenic inputs. Hence, our study highlights
1023 the importance for undertaking biogeochemical process-oriented studies at the scale of
1024 hydrothermal plumes and integrating geological and hydrological parameters into those
1025 studies.

1026

1027 **Acknowledgments**

1028 We thank Diane Adams and Lauren Mullineaux for sediment trap deployments at the EPR
1029 and Bill Seyfried for providing hydrothermal fluid samples from the oceanographic cruise
1030 AT-15. Support for sediment trap analysis was funded by OCE-0647948, awarded to CRG
1031 and OJR. We thank Maureen Auro for laboratory assistance at WHOI, Lary Ball and
1032 Emmanuel Ponzevera for daily maintenance of the MC-ICPMS and Yoan Germain for help
1033 with hydrothermal fluid analysis. We thank Bill Seyfried and Andrea Thurnherr for their
1034 helpful comments on the manuscript. Financial support for this work was also provided by the
1035 Labex Mer (ANR-10-LABX-19-01), Europe Mer and FP7 (#247837) grants to OJR. We
1036 thank M.A. Marcus for research support at the Advanced Light Source beamline 10.3.2. The
1037 Advanced Light Source is supported by the Office of Science, Basic Energy Sciences,
1038 Division of Materials Science of the U.S. Department of Energy (DE-AC02-05CH11231).

1039

1040

1041

1042

1043

1044

1045

1046

1047 **REFERENCES**

1048

- 1049 Adams, D.K., McGillicuddy, D.J., Zamudio, L., Thurnherr, A.M., Liang, X.F., Rouxel, O., German,
1050 C.R., Mullineaux, L.S., 2011. Surface-Generated Mesoscale Eddies Transport Deep-Sea
1051 Products from Hydrothermal Vents. *Science*, 332(6029): 580-583.
- 1052 Baker, E.T., 1994. A 6-year time series of hydrothermal plumes over the Cleft segment of the Juan de
1053 Fuca Ridge. *J. Geophys. Res.-Solid Earth*, 99(B3): 4889-4904.
- 1054 Baker, E.T., Chadwick, W.W., Cowen, J.P., Dziak, R.P., Rubin, K.H., Fornari, D.J., 2012.
1055 Hydrothermal Discharge During Submarine Eruptions: The Importance of Detection,
1056 Response, and New Technology. *Oceanography*, 25(1): 128-141.
- 1057 Baker, E.T., Massoth, G.J., Feely, R.A., 1987. Cataclysmic hydrothermal venting on the Juan de Fuca
1058 Ridge. *Nature*, 329(6135): 149-151.
- 1059 Balci, N., Bullen, T.D., Witte-Lien, K., Shanks, W.C., Motelica, M., Mandernack, K.W., 2006. Iron
1060 isotope fractionation during microbially stimulated Fe(II) oxidation and Fe(III) precipitation.
1061 *Geochim. Cosmochim. Acta*, 70(3): 622-639.
- 1062 Banks, R., 1979. The use of linear programming in the analysis of petrological mixing problems.
1063 *Contrib. Mineral. Petrol.*, 70(3): 237-244.
- 1064 Baumberger, T., Lilley, M.D., Resing, J.A., Lupton, J.E., Baker, E.T., Butterfield, D.A., Olson, E.J.,
1065 Fruh-Green, G.L., 2014. Understanding a submarine eruption through time series
1066 hydrothermal plume sampling of dissolved and particulate constituents: West Mata, 2008–
1067 2012. *Geochem Geophys Geosy*, 15: doi:10.1002/2014GC005460.
- 1068 Beard, B.L., Johnson, C.M., Skulan, J.L., Neelson, K.H., Cox, L., Sun, H., 2003a. Application of Fe
1069 isotopes to tracing the geochemical and biological cycling of Fe. *Chem. Geol.*, 195(1-4): 87-
1070 117.
- 1071 Beard, B.L., Johnson, C.M., Von Damm, K.L., Poulson, R.L., 2003b. Iron isotope constraints on Fe
1072 cycling and mass balance in oxygenated Earth oceans. *Geology*, 31(7): 629-632.
- 1073 Bennett, S.A., Achterberg, E.P., Connelly, D.P., Statham, P.J., Fones, G.R., German, C.R., 2008. The
1074 distribution and stabilisation of dissolved Fe in deep-sea hydrothermal plumes. *Earth. Planet.
1075 Sci. Lett.*, 270: 157-167.
- 1076 Bennett, S.A., Hansman, R.L., Sessions, A.L., Nakamura, K., Edwards, K.J., 2011a. Tracing iron-
1077 fueled microbial carbon production within the hydrothermal plume at the Loihi seamount.
1078 *Geochim. Cosmochim. Acta*, 75: 5526–5539.
- 1079 Bennett, S.A., Rouxel, O., Schmidt, K., Garbe-Schonberg, D., Statham, P.J., German, C.R., 2009. Iron
1080 isotope fractionation in a buoyant hydrothermal plume, 5 degrees S Mid-Atlantic Ridge.
1081 *Geochim. Cosmochim. Acta*, 73(19): 5619-5634.
- 1082 Bennett, S.A., Statham, P.J., Green, D.R.H., Le Bris, N., McDermott, J.M., Prado, F., Rouxel, O.J.,
1083 Von Damm, K., German, C.R., 2011b. Dissolved and particulate organic carbon in

- 1084 hydrothermal plumes from the East Pacific Rise, 9 degrees 50 ' N. Deep Sea Res. (I Oceanogr.
1085 Res. Pap.), 58(9): 922-931.
- 1086 Bergquist, B.A., Boyle, E.A., 2006. Iron isotopes in the Amazon River system: Weathering and
1087 transport signatures. Earth. Planet. Sci. Lett., 248(1-2): 54-68.
- 1088 Berner, R.A., Honjo, S., 1981. Pelagic Sedimentation of Aragonite: Its Geochemical Significance.
1089 Science, 211(4485): 940-942.
- 1090 Blanchard, M., Poitrasson, F., Meheut, M., Lazzeri, M., Mauri, F., Balan, E., 2009. Iron isotope
1091 fractionation between pyrite (FeS₂), hematite (Fe₂O₃) and siderite (FeCO₃): A first-principles
1092 density functional theory study. Geochim. Cosmochim. Acta, 73(21): 6565-6578.
- 1093 Blanchard, M., Poitrasson, F., Meheut, M., Lazzeri, M., Mauri, F., Balan, E., 2012. Comment on
1094 "New data on equilibrium iron isotope fractionation among sulfides: Constraints on
1095 mechanisms of sulfide formation in hydrothermal and igneous systems" by VB Polyakov and
1096 DM Soultanov. Geochim. Cosmochim. Acta, 87: 356-359.
- 1097 Boyle, E.A., John, S., Abouchami, W., Adkins, J.F., Echegoyen-Sanz, Y., Ellwood, M., Flegal, A.R.,
1098 Fornace, K., Gallon, C., Galer, S., Gault-Ringold, M., Lacan, F., Radic, A., Rehkämper, M.,
1099 Rouxel, O., Sohrin, Y., Stirling, C., Thompson, C., Vance, D., Xue, Z.C., Zhao, Y., 2012.
1100 GEOTRACES IC1 (BATS) contamination-prone trace element isotopes Cd, Fe, Pb, Zn, Cu,
1101 and Mo intercalibration. Limnol Oceanogr-Meth, 10: 653-665.
- 1102 Breier, J.A., Toner, B.M., Fakra, S.C., Marcus, M.A., White, S.N., Thurnherr, A.M., German, C.R.,
1103 2012. Sulfur, sulfides, oxides and organic matter aggregated in submarine hydrothermal
1104 plumes at 9 degrees 50 ' N East Pacific Rise. Geochim. Cosmochim. Acta, 88: 216-236.
- 1105 Brown, S.J., Elderfield, H., 1996. Variations in Mg/Ca and Sr/Ca ratios of planktonic foraminifera
1106 caused by postdepositional dissolution: Evidence of shallow Mg-dependent dissolution.
1107 Paleoceanography, 11(5): 543-551.
- 1108 Buesseler, K.O., Antia, A.N., Chen, M., Fowler, S.W., Gardner, W.D., Gustafsson, O., Harada, K.,
1109 Michaels, A.F., van der Loeff'o, M.R., Sarin, M., Steinberg, D.K., Trull, T., 2007. An
1110 assessment of the use of sediment traps for estimating upper ocean particle fluxes. J. Mar.
1111 Res., 65(3): 345-416.
- 1112 Bullen, T.D., White, A.F., Childs, C.W., Vivit, D.V., Schulz, M.S., 2001. Demonstration of significant
1113 abiotic iron isotope fractionation in nature. Geology, 29: 699-702.
- 1114 Butler, I.B., Archer, C., Vance, D., Oldroyd, A., Rickard, D., 2005. Fe isotope fractionation on FeS
1115 formation in ambient aqueous solution. Earth. Planet. Sci. Lett., 236: 430-442.
- 1116 Carazzo, G., Jellinek, A.M., Turchyn, A.V., 2013. The remarkable longevity of submarine plumes:
1117 Implications for the hydrothermal input of iron to the deep-ocean. Earth. Planet. Sci. Lett.,
1118 382: 66-76.
- 1119 Cave, R.R., German, C.R., Thomson, J., Nesbitt, R.W., 2002. Fluxes to sediments underlying the
1120 Rainbow hydrothermal plume at 36 degrees 14 ' N on the Mid-Atlantic Ridge. Geochim.
1121 Cosmochim. Acta, 66(11): 1905-1923.

- 1122 Chu, N.C., Johnson, C.M., Beard, B.L., German, C.R., Nesbitt, R.W., Frank, M., Bohn, M., Kubik,
1123 P.W., Usui, A., Graham, I., 2006. Evidence for hydrothermal venting in Fe isotope
1124 compositions of the deep Pacific Ocean through time. *Earth. Planet. Sci. Lett.*, 245(1-2): 202-
1125 217.
- 1126 Cohen, D., Ward, C.R., 1991. SEDNORM—a program to calculate a normative mineralogy for
1127 sedimentary rocks based on chemical analyses. *Computers & Geosciences*, 17(9): 1235-1253.
- 1128 Conway, T.M., John, S.G., 2014. Quantification of dissolved iron sources to the North Atlantic Ocean.
1129 *Nature*, 511(7508): 212-216.
- 1130 Cowen, J.P., Bertram, M.A., Wakeham, S.G., Thomson, R.E., Lavelle, J.W., Baker, E.T., Feely, R.A.,
1131 2001. Ascending and descending particle flux from hydrothermal plumes at Endeavour
1132 Segment, Juan de Fuca Ridge. *Deep Sea Res. (I Oceanogr. Res. Pap.)*, 48(4): 1093-1120.
- 1133 Cowen, J.P., Massoth, G.J., Baker, E.T., 1986. Bacterial scavenging of Mn and Fe in a mid- to far-
1134 field hydrothermal particle plume. *Nature*, 322(6075): 169-171.
- 1135 Cowen, J.P., Massoth, G.J., Feely, R.A., 1990. Scavenging rates of dissolved manganese in a
1136 hydrothermal vent plume. *Deep Sea Res. (I Oceanogr. Res. Pap.)*, 37(10): 1619-1637.
- 1137 Cronan, D.S., Hodkinson, R.A., 1997. Geochemistry of hydrothermal sediments from ODP sites 834
1138 and 835 in the Lau Basin, southwest Pacific. *Mar. Geol.*, 141(1-4): 237-268.
- 1139 DeAngelis, M.A., Lilley, M.D., Olson, E.J., Baross, J.A., 1993. Methane oxidation in deep-sea
1140 hydrothermal plumes of the Endeavour Segment of the Juan de Fuca Ridge. *Deep Sea Res. (I
1141 Oceanogr. Res. Pap.)*, 40(6): 1169-1186.
- 1142 Detrick, R.S., Buhl, P., Vera, E., Mutter, J., Orcutt, J., Madsen, J., Brocher, T., 1987. Multi-channel
1143 seismic imaging of a crustal magma chamber along the East Pacific Rise. *Nature*, 326: 35-41.
- 1144 Dick, G.J., Anantharaman, K., Baker, B.J., Li, M., Reed, D.C., Sheik, C.S., 2013. The microbiology of
1145 deep-sea hydrothermal vent plumes: ecological and biogeographic linkages to seafloor and
1146 water column habitats. *Frontiers in Microbiology*, 4.
- 1147 Dick, G.J., Tebo, B.M., 2010. Microbial diversity and biogeochemistry of the Guaymas Basin deep-
1148 sea hydrothermal plume. *Environ. Microbiol.*, 12(5): 1334-1347.
- 1149 Dymond, J., Roth, S., 1988. Plume dispersed hydrothermal particles: A time-series record of settling
1150 flux from the Endeavour Ridge using moored sensors. *Geochim. Cosmochim. Acta*, 52(10):
1151 2525-2536.
- 1152 Dymond, J., Suess, E., Lyle, M., 1992. Barium in deep-sea sediments: a geochemical proxy for
1153 paleoproductivity. *Paleoceanography*, 7(2): 163-181.
- 1154 Edmond, J.M., Measures, C.I., McDuff, R.E., Chan, L.H., Collier, R., Grant, B., Gordon, L.I., Corliss,
1155 J.B., 1979. Ridge crest hydrothermal activity and the balances of the major and minor
1156 elements in the ocean: the Galapagos data. *Earth. Planet. Sci. Lett.*, 46: 1-18.

- 1157 Edmond, J.M., Von Damm, K.L., McDuff, R.E., Measures, C.I., 1982. Chemistry of hot springs on the
1158 East Pacific Rise and their effluent dispersal. *Nature*, 297(5863): 187-191.
- 1159 Elderfield, H., Mills, R.A., Rudnicki, M.D., 1993. Geochemical and thermal fluxes, high-temperature
1160 venting and diffuse flow from mid-ocean ridge hydrothermal systems; the TAG hydrothermal
1161 field, Mid-Atlantic Ridge 26 degrees N. *Geological Society Special Publications*, 76: 295-307.
- 1162 Elderfield, H., Schultz, A., 1996. Mid-ocean ridge hydrothermal fluxes and the chemical composition
1163 of the ocean. *Ann. Rev. Earth Planet. Sci.*, 24: 191-224.
- 1164 Escoube, R., Rouxel, O.J., Sholkovitz, E., Donard, O.F.X., 2009. Iron isotope systematics in estuaries:
1165 The case of North River, Massachusetts (USA). *Geochim. Cosmochim. Acta*, 73(14): 4045-
1166 4059.
- 1167 Feely, R.A., Baker, E.T., Marumo, K., Urabe, T., Ishibashi, J., Gendron, J., Lebon, G.T., Okamura, K.,
1168 1996. Hydrothermal plume particles and dissolved phosphate over the superfast-spreading
1169 southern East Pacific Rise. *Geochim. Cosmochim. Acta*, 60(13): 2297-2323.
- 1170 Feely, R.A., Gendron, J.F., Baker, E.T., Lebon, G.T., 1994. Hydrothermal plumes along the East
1171 Pacific Rise, 8°40' to 11°50'N: plume distribution and composition. *Earth. Planet. Sci. Lett.*,
1172 128(1-2): 19-36.
- 1173 Feely, R.A., Massoth, G.J., Baker, E.T., Cowen, J.P., Lamb, M.F., Kroglund, K.A., 1990. The effect
1174 of hydrothermal processes on midwater phosphorus distributions in the northeast Pacific.
1175 *Earth. Planet. Sci. Lett.*, 96(3-4): 305-318.
- 1176 Feely, R.A., Trefry, J.H., Lebon, G.T., German, C.R., 1998. The relationship between P/Fe and V/Fe
1177 ratios in hydrothermal precipitates and dissolved phosphate in seawater. *Geophys. Res. Lett.*,
1178 25(13): 2253-2256.
- 1179 Feely, R.A., Trefry, J.H., Massoth, G.J., Metz, S., 1991. A comparison of the scavenging of
1180 phosphorus and arsenic from seawater by hydrothermal iron oxyhydroxides in the Atlantic
1181 and Pacific Oceans. *Deep Sea Res. (I Oceanogr. Res. Pap.)*, 38(6): 617-623.
- 1182 Fitzsimmons, J., Conway, T., John, S., Boyle, E., 2013. Iron Isotopes in Seawater from the Southeast
1183 Pacific and North Atlantic Oceans. *Mineralogical Magazine*, 77((5)): 1092.
- 1184 Fitzsimmons, J.N., Boyle, E.A., Jenkins, W.J., 2014. Distal transport of dissolved hydrothermal iron in
1185 the deep South Pacific Ocean. *Proc. Natl. Acad. Sci. USA*, 111(47).
- 1186 Fornari, D.J., Shank, T., Von Damm, K.L., Gregg, T.K.P., Lilley, M., Levai, G., Bray, A., Haymon,
1187 R.M., Perfit, M.R., Lutz, R., 1998. Time-series temperature measurements at high-temperature
1188 hydrothermal vents, East Pacific Rise 9 degrees 49 '-51 ' N: evidence for monitoring a crustal
1189 cracking event. *Earth. Planet. Sci. Lett.*, 160(3-4): 419-431.
- 1190 Fornari, D.J., Von Damm, K.L., Bryce, J.G., Cowen, J.P., Ferrini, V., Fundis, A., Lilley, M.D., Luther,
1191 G.W., Mullineaux, L.S., Perfit, M.R., Meana-Prado, M.F., Rubin, K.H., Seyfried, W.E.,
1192 Shank, T.M., Soule, S.A., Tolstoy, M., White, S.M., 2012. The East Pacific Rise Between 9
1193 degrees N and 10 degrees N: Twenty-Five Years of Integrated, Multidisciplinary Oceanic
1194 Spreading Center Studies. *Oceanography*, 25(1): 18-+.

- 1195 Gartman, A., Findlay, A.J., Luther, G.W., 2014. Nanoparticulate pyrite and other nanoparticles are a
1196 widespread component of hydrothermal vent black smoker emissions. *Chem. Geol.*, 366: 32-
1197 41.
- 1198 German, C., Petersen, S., Hannington, M.D., 2016. Hydrothermal exploration of mid-ocean ridges:
1199 Where might the largest sulfide deposits occur? . *Chem. Geol.*, 420(1): 114-126.
- 1200 German, C., Seyfried, W.E., 2014. 8.7 – Hydrothermal Processes. *Treatise on Geochemistry (Second*
1201 *Edition)*, 8: 191–233.
- 1202 German, C.R., Bourles, D.L., Brown, E.T., Hergt, J., Colley, S., Higgs, N.C., Ludford, E.M., Nelsen,
1203 T.A., Feely, R.A., Raisbeck, G., Yiou, F., 1997. Hydrothermal scavenging on the Juan de
1204 Fuca Ridge: Th-230(xs), Be-10, and REEs in ridge-flank sediments. *Geochim. Cosmochim.*
1205 *Acta*, 61(19): 4067-4078.
- 1206 German, C.R., Campbell, A.C., Edmond, J.M., 1991a. Hydrothermal scavenging at the Mid-Atlantic
1207 Ridge: Modification of trace element dissolved fluxes. *Earth. Planet. Sci. Lett.*, 107(1): 101-
1208 114.
- 1209 German, C.R., Colley, S., Palmer, M.R., Khripounoff, A., Klinkhammer, G.P., 2002. Hydrothermal
1210 plume-particle fluxes at 13 degrees N on the East Pacific Rise. *Deep Sea Res. (I Oceanogr.*
1211 *Res. Pap.)*, 49(11): 1921-1940.
- 1212 German, C.R., Fler, A.P., Bacon, M.P., Edmond, J.M., 1991b. Hydrothermal scavenging at the Mid-
1213 Atlantic Ridge: radionuclide distributions. *Earth. Planet. Sci. Lett.*, 105(1-3): 170-181.
- 1214 German, C.R., Legendre, L.L., Sander, S.G., Niquil, N., Luther, G.W., Bharati, L., Han, X., Le Bris,
1215 N., 2015. Hydrothermal Fe cycling and deep ocean organic carbon scavenging: Model-based
1216 evidence for significant POC supply to seafloor sediments. *Earth. Planet. Sci. Lett.*, 419: 143-
1217 153.
- 1218 German, C.R., Thurnherr, A.M., Knoery, J., Charlou, J.L., Jean-Baptiste, P., Edmonds, H.N., 2010.
1219 Heat, volume and chemical fluxes from submarine venting: A synthesis of results from the
1220 Rainbow hydrothermal field, 36 degrees N MAR. *Deep Sea Res. (I Oceanogr. Res. Pap.)*,
1221 57(4): 518-527.
- 1222 German, C.R., Von Damm, K.L., 2003. Hydrothermal Processes. In: Elderfield, H. (Ed.), *Treatise on*
1223 *Geochemistry*. Elsevier, pp. 181-222.
- 1224 Goss, A.R., Perfit, M.R., Ridley, W.I., Rubin, K.H., Kamenov, G.D., Soule, S.A., Fundis, A., Fornari,
1225 D.J., 2010. Geochemistry of lavas from the 2005-2006 eruption at the East Pacific Rise, 9
1226 degrees 46 ' N-9 degrees 56 ' N: Implications for ridge crest plumbing and decadal changes in
1227 magma chamber compositions. *Geochem Geophys Geosy*, 11.
- 1228 Guilbaud, R., Butler, I.B., Ellam, R.M., Rickard, D., Oldroyd, A., 2011. Experimental determination
1229 of the equilibrium Fe isotope fractionation between Fe-aq(2+) and FeSm (mackinawite) at 25
1230 and 2 degrees C. *Geochim. Cosmochim. Acta*, 75(10): 2721-2734.
- 1231 Haymon, R.M., Fornari, D.J., Edwards, M.H., Carbotte, S., Wright, D., Macdonald, K.C., 1991.
1232 Hydrothermal vent distribution along the East Pacific Rise crest (9°09'-54'N) and its

- 1233 relationship to magmatic and tectonic processes on fast-spreading mid-ocean ridges. *Earth.*
1234 *Planet. Sci. Lett.*, 104: 513-534.
- 1235 Haymon, R.M., Fornari, D.J., Von Damm, K.L., Lilley, M.D., Perfit, M.R., Edmond, J.M., Shanks,
1236 W.C., Lutz, R.A., Grebmeier, J.M., Carbotte, S., Wright, D., McLaughlin, E., Smith, M.,
1237 Beedle, N., Olson, E., 1993. Volcanic eruption of the mid-ocean ridge along the East Pacific
1238 Rise crest at 9°45–52°N: Direct submersible observations of seafloor phenomena associated
1239 with an eruption event in April, 1991. *Earth. Planet. Sci. Lett.*, 119(1-2): 85-101.
- 1240 Hernes, P.J., Peterson, M.L., Murray, J.W., Wakeham, S.G., Lee, C., Hedges, J.I., 2001. Particulate
1241 carbon and nitrogen fluxes and compositions in the central equatorial Pacific. *Deep Sea Res.*
1242 *(I Oceanogr. Res. Pap.)*, 48(9): 1999-2023.
- 1243 Honjo, S., Dymond, J., Collier, R., Manganini, S.J., 1995. Export production of particles to the interior
1244 of the equatorial Pacific Ocean during the 1992 EqPac experiment. *Deep Sea Res. (II Top.*
1245 *Stud. Oceanogr.)*, 42(2-3): 831-870.
- 1246 Horner, T.J., Williams, H.M., Hein, J.R., Saito, M.A., Burton, K.W., Halliday, A.N., Nielsen, S.G.,
1247 2015. Persistence of deeply sourced iron in the Pacific Ocean. *Proc. Natl. Acad. Sci. USA*,
1248 112(5): 1292-1297.
- 1249 Jickells, T.D., Deuser, W.G., Knap, A.H., 1984. The sedimentation rates of trace elements in the
1250 Sargasso Sea measured by sediment trap. *Deep Sea Res. (I Oceanogr. Res. Pap.)*, 31(10):
1251 1169-1178.
- 1252 John, S.G., Adkins, J., 2012. The vertical distribution of iron stable isotopes in the North Atlantic near
1253 Bermuda. *Global Biogeochem. Cycles*, 26.
- 1254 John, S.G., Adkins, J.F., 2010. Analysis of dissolved iron isotopes in seawater. *Mar. Chem.*, 119(1-4):
1255 65-76.
- 1256 John, S.G., Conway, T.M., 2014. A role for scavenging in the marine biogeochemical cycling of zinc
1257 and zinc isotopes. *Earth. Planet. Sci. Lett.*, 394: 159-167.
- 1258 Kadko, D., 1993. An assessment of the effect of chemical scavenging within submarine hydrothermal
1259 plumes upon ocean geochemistry. *Earth. Planet. Sci. Lett.*, 120(3-4): 361-374.
- 1260 Kadko, D., Feely, R., Massoth, G., 1994. Scavenging of ²³⁴Th and phosphorous removal from the
1261 hydrothermal effluent plume over the North Cleft segment of the Juan de Fuca Ridge. *J.*
1262 *Geophys. Res.-Solid Earth*, 99(B3): 5017-5024.
- 1263 Klevenz, V., Bach, W., Schmidt, K., Hentscher, M., Koschinsky, A., Petersen, S., 2011. Geochemistry
1264 of vent fluid particles formed during initial hydrothermal fluid-seawater mixing along the
1265 Mid-Atlantic Ridge. *Geochem Geophys Geosy*, 12.
- 1266 Klunder, M.B., Laan, P., Middag, R., de Baar, H.J.W., Bakker, K., 2012. Dissolved iron in the Arctic
1267 Ocean: Important role of hydrothermal sources, shelf input and scavenging removal. *J.*
1268 *Geophys. Res.*, 117.

- 1269 Kraft, S., Stümpel, J., Becker, P., Kuetsgens, U., 1996. High resolution x-ray absorption spectroscopy
1270 with absolute energy Calibration for the determination of absorption edge energies. *Rev. Sci.*
1271 *Instrum.*, 67: 681–687.
- 1272 Lacan, F., Radic, A., Jeandel, C., Poitrasson, F., Sarthou, G., Pradoux, C., Freydier, R., 2008.
1273 Measurement of the isotopic composition of dissolved iron in the open ocean. *Geophys. Res.*
1274 *Lett.*, 35(24).
- 1275 Lacan, F., Radic, A., Labatut, M., Jeandel, C., Poitrasson, F., Sarthou, G., Pradoux, C., Chmeleff, J.,
1276 Freydier, R., 2010. High-Precision Determination of the Isotopic Composition of Dissolved
1277 Iron in Iron Depleted Seawater by Double Spike Multicollector-ICPMS. *Anal Chem*, 82(17):
1278 7103-7111.
- 1279 Lam, P., Cowen, J.P., Popp, B.N., Jones, R.D., 2008. Microbial ammonia oxidation and enhanced
1280 nitrogen cycling in the Endeavour hydrothermal plume. *Geochim. Cosmochim. Acta*, 72(9):
1281 2268-2286.
- 1282 Lamborg, C.H., Buesseler, K.O., Lam, P.J., 2008. Sinking fluxes of minor and trace elements in the
1283 North Pacific Ocean measured during the VERTIGO program. *Deep Sea Res. (II Top. Stud.*
1284 *Oceanogr.)*, 55(14-15): 1564-1577.
- 1285 Li, M., Toner, B.M., Baker, B.J., Breier, J.A., Sheik, C.S., Dick, G.J., 2014. Microbial iron uptake as a
1286 mechanism for dispersing iron from deep-sea hydrothermal vents. *Nature Communications*, 5.
- 1287 Liang, X.F., Thurnherr, A.M., 2011. Subinertial variability in the deep ocean near the East Pacific
1288 Rise between 9 degrees and 10 degrees N. *Geophys. Res. Lett.*, 38.
- 1289 Liang, X.F., Thurnherr, A.M., 2012. Eddy-Modulated Internal Waves and Mixing on a Mid-ocean
1290 Ridge. *J. Phys. Oceanogr.*, 42(7): 1242-1248.
- 1291 Lupton, J.E., Baker, E.T., Garfield, N., Massoth, G.J., Feely, R.A., Cowen, J.P., Greene, R.R., Rago,
1292 T.A., 1998. Tracking the evolution of a hydrothermal event plume with a RAFOS neutrally
1293 buoyant drifter. *Science*, 280(5366): 1052-1055.
- 1294 Manceau, A., Marcus, M.A., Tamura, N., 2002. Quantitative speciation of heavy metals in soils and
1295 sediments by synchrotron x-ray techniques. In: Fenter, P.A., Rivers, M.L., Sturchio, N.C.,
1296 Sutton, S.R. (Eds.), *Applications of synchrotron radiation in low-temperature geochemistry*
1297 *and environmental science*. Mineralogical Society of America, Washington D.C.
- 1298 Mandernack, K.W., Tebo, B.M., 1993. Manganese scavenging and oxidation at hydrothermal vents
1299 and in vent plumes. *Geochim. Cosmochim. Acta*, 57(16): 3907-3923.
- 1300 Marcus, M.A., MacDowell, A., Celestre, R., Manceau, A., Miller, T., Padmore, H.A., Sublett, R.E.,
1301 2004. Beamline 10.3.2 at ALS: a hard X-ray microprobe for environmental and material
1302 sciences. *J. Synchrotron Rad.*, 11: 239-247.
- 1303 Marcus, M.A., Westphal, A.J., Fakra, S., 2008. Classification of Fe-bearing species from K-edge
1304 XANES data using two-parameter correlation plots. *J. Synchrotron Rad.*, 15: 463-468.

- 1305 McGillicuddy, D.J., Lavelle, J.W., Thurnherr, A.M., Kosnyrev, V.K., Mullineaux, L.S., 2010. Larval
 1306 dispersion along an axially symmetric mid-ocean ridge. *Deep-Sea Research Part I-*
 1307 *Oceanographic Research Papers*, 57(7): 880-892.
- 1308 Mills, R.A., Elderfield, H., 1995. Rare earth element geochemistry of hydrothermal deposits from the
 1309 active TAG mound, 26°N Mid-Atlantic Ridge. *Geochim. Cosmochim. Acta*, 59: 3511-3524.
- 1310 Mills, R.A., Taylor, S.L., Palike, H., Thomson, J., 2010. Hydrothermal sediments record changes in
 1311 deep water oxygen content in the SE Pacific. *Paleoceanography*, 25.
- 1312 Mottl, M.J., McConachy, T.F., 1990. Chemical processes in buoyant hydrothermal plumes on the East
 1313 Pacific Rise near 21°N. *Geochim. Cosmochim. Acta*, 54(7): 1911-1927.
- 1314 Mullineaux, L.S., Adams, D.K., Mills, S.W., Beaulieu, S.E., 2010. Larvae from afar colonize deep-sea
 1315 hydrothermal vents after a catastrophic eruption. *Proc. Natl. Acad. Sci. USA*, 107(17): 7829-
 1316 7834.
- 1317 Nishioka, J., Obata, H., Tsumune, D., 2013. Evidence of an extensive spread of hydrothermal
 1318 dissolved iron in the Indian Ocean. *Earth. Planet. Sci. Lett.*, 361: 26-33.
- 1319 O'Brien, D., Carton, M., Eardly, D., Patching, J.W., 1998. In situ filtration and preliminary molecular
 1320 analysis of microbial biomass from the Rainbow hydrothermal plume at 36 degrees 15 ' N on
 1321 the Mid-Atlantic Ridge. *Earth. Planet. Sci. Lett.*, 157(3-4): 223-231.
- 1322 Pester, N.J., Ding, K., Seyfried, W.E., 2014. Magmatic eruptions and iron volatility in deep-sea
 1323 hydrothermal fluids. *Geology*, 42(3): 255-258.
- 1324 Pester, N.J., Rough, M., Ding, K., Seyfried, W.E., 2011. A new Fe/Mn geothermometer for
 1325 hydrothermal systems: Implications for high-salinity fluids at 13 degrees N on the East Pacific
 1326 Rise. *Geochim. Cosmochim. Acta*, 75(24): 7881-7892.
- 1327 Plank, T., Langmuir, C.H., 1998. The chemical composition of subducting sediment and its
 1328 consequences for the crust and mantle. *Chem. Geol.*, 145: 325-394.
- 1329 Polyakov, V.B., Soultanov, D.M., 2011. New data on equilibrium iron isotope fractionation among
 1330 sulfides: Constraints on mechanisms of sulfide formation in hydrothermal and igneous
 1331 systems. *Geochim. Cosmochim. Acta*, 75(7): 1957-1974.
- 1332 Pruseth, K.L., 2009. MATNORM: Calculating NORM using composition matrices. *Computers &*
 1333 *Geosciences*, 35(9): 1785-1788.
- 1334 Radic, A., Lacan, F., Murray, J.W., 2011. Iron isotopes in the seawater of the equatorial Pacific
 1335 Ocean: New constraints for the oceanic iron cycle. *Earth. Planet. Sci. Lett.*, 306(1-2): 1-10.
- 1336 Resing, J.A., Sedwick, P.N., German, C.R., Jenkins, W.J., Moffett, J.W., Sohst, B.M., Tagliabue, A.,
 1337 2015. Basin-scale transport of hydrothermal dissolved metals across the South Pacific Ocean.
 1338 *Nature*, 523(7559): 200-U140.

- 1339 Revels, B.N., Ohnemus, D.C., Lam, P.J., Conway, T.M., John, S.G., 2015. The isotopic signature and
 1340 distribution of particulate iron in the North Atlantic Ocean. *Deep-Sea Research Part II-Topical*
 1341 *Studies in Oceanography*, 116: 321-331.
- 1342 Roshan, S., Wu, J.F., Jenkins, W.J., 2016. Long-range transport of hydrothermal dissolved Zn in the
 1343 tropical South Pacific. *Mar. Chem.*, 183: 25-32.
- 1344 Roth, S.E., Dymond, J., 1989. Transport and settling of organic material in a deep-sea hydrothermal
 1345 plume: evidence from particle flux measurements. *Deep Sea Res. (I Oceanogr. Res. Pap.)*,
 1346 36(8): 1237-1254.
- 1347 Rouxel, O., Dobbek, N., Ludden, J., Fouquet, Y., 2003. Iron isotope fractionation during oceanic crust
 1348 alteration. *Chem. Geol.*, 202(1-2): 155-182.
- 1349 Rouxel, O., Fouquet, Y., Ludden, J.N., 2004. Subsurface processes at the Lucky Strike hydrothermal
 1350 field, Mid-Atlantic Ridge: Evidence from sulfur, selenium, and iron isotopes. *Geochim.*
 1351 *Cosmochim. Acta*, 68(10): 2295-2311.
- 1352 Rouxel, O., Shanks, W.C., Bach, W., Edwards, K.J., 2008a. Integrated Fe- and S-isotope study of
 1353 seafloor hydrothermal vents at East Pacific Rise 9-10°N. *Chem. Geol.*, 252(3-4): 214-227.
- 1354 Rouxel, O., Sholkovitz, E., Charette, M., Edwards, K.J., 2008b. Iron isotope fractionation in
 1355 subterranean estuaries. *Geochim. Cosmochim. Acta*, 72(14): 3413-3430.
- 1356 Rouxel, O.J., Auro, M., 2010. Iron Isotope Variations in Coastal Seawater Determined by
 1357 Multicollector ICP-MS. *Geostand. Geoanal. Res.*, 34(2): 135-144.
- 1358 Rudnicki, M.D., Elderfield, H., 1993. A chemical model of the buoyant and neutrally buoyant plume
 1359 above the TAG vent field, 26 degrees N, Mid-Atlantic Ridge. *Geochim. Cosmochim. Acta*,
 1360 57: 2939-2957.
- 1361 Ruhlin, D.E., Owen, R.M., 1986. The rare earth element geochemistry of hydrothermal sediments
 1362 from the East Pacific Rise: Examination of a seawater scavenging mechanism. *Geochim.*
 1363 *Cosmochim. Acta*, 50(3): 393-400.
- 1364 Saito, M.A., Noble, A.E., Tagliabue, A., Goepfert, T.J., Lamborg, C.H., Jenkins, W.J., 2013. Slow-
 1365 spreading submarine ridges in the South Atlantic as a significant oceanic iron source. *Nature*
 1366 *Geoscience*, 6(9): 775-779.
- 1367 Sander, S.G., Koschinsky, A., 2011. Metal flux from hydrothermal vents increased by organic
 1368 complexation. *Nature Geoscience*, 4(3): 145-150.
- 1369 Santelli, C.M., Orcutt, B.N., Banning, E., Bach, W., Moyer, C.L., Sogin, M.L., Staudigel, H.,
 1370 Edwards, K.J., 2008. Abundance and diversity of microbial life in ocean crust. *Nature*,
 1371 453(7195): 653-657.
- 1372 Seewald, J.S., Doherty, K.W., Hammar, T.R., Liberatore, S.P., 2002. A new gas-tight isobaric sampler
 1373 for hydrothermal fluids. *Deep Sea Res. (I Oceanogr. Res. Pap.)*, 49: 189-196.

- 1374 Severmann, S., Johnson, C.M., Beard, B.L., German, C.R., Edmonds, H.N., Chiba, H., Green, D.R.H.,
1375 2004. The effect of plume processes on the Fe isotope composition of hydrothermally derived
1376 Fe in the deep ocean as inferred from the Rainbow vent site, Mid-Atlantic Ridge, 36 degrees
1377 14' N. *Earth. Planet. Sci. Lett.*, 225(1-2): 63-76.
- 1378 Severmann, S., Johnson, C.M., Beard, B.L., McManus, J., 2006. The effect of early diagenesis on the
1379 Fe isotope compositions of porewaters and authigenic minerals in continental margin
1380 sediments. *Geochim. Cosmochim. Acta*, 70(8): 2006-2022.
- 1381 Shank, T.M., Fornari, D.J., Van Damm, K.L., Lilley, M.D., Haymon, R.M., Lutz, R.A., 1998.
1382 Temporal and spatial patterns of biological community development at nascent deep-sea
1383 hydrothermal vents (9°50'N, East Pacific Rise). *Deep Sea Res. (II Top. Stud. Oceanogr.)*, 45:
1384 465-515.
- 1385 Shanks, W.C., 2001. Stable isotopes in seafloor hydrothermal systems: vent fluids, hydrothermal
1386 deposits, hydrothermal alteration, and microbial processes. *Reviews in Mineralogy and
1387 Geochemistry*, 43: 469-525.
- 1388 Shanks, W.C., Böhlke, J.K., Seal, R.R., 1995. Stable Isotopes in Mid-Ocean Ridge Hydrothermal
1389 Systems: Interactions between Fluids, Minerals, and Organisms. In: Humphris, S.E.,
1390 Zierenberg, R.A., Mullineaux, L.S., Thomson, R.E. (Eds.), *Seafloor Hydrothermal System:
1391 Physical, Chemical, Biological and Geological Interactions*, pp. 194-221.
- 1392 Sharma, M., Polizzotto, M., Anbar, A.D., 2001. Iron isotopes in hot springs along the Juan de Fuca
1393 Ridge. *Earth. Planet. Sci. Lett.*, 194: 39-51.
- 1394 Siegel, D.A., Deuser, W.G., 1997. Trajectories of sinking particles in the Sargasso Sea: modeling of
1395 statistical funnels above deep-ocean sediment traps. *Deep Sea Res. (I Oceanogr. Res. Pap.)*,
1396 44(9-10): 1519-1541.
- 1397 Soule, S.A., Fornari, D.J., Perfit, M.R., Rubin, K.H., 2007. New insights into mid-ocean ridge
1398 volcanic processes from the 2005-06 eruption of the East Pacific Rise, 9°46'N-9°56'N.
1399 *Geology*, 35: 1079-1082.
- 1400 Stein, C.A., Stein, S., 1994. Constraints on hydrothermal heat flux through the oceanic lithosphere
1401 from global heat flow. *J. Geophys. Res.*, 99: 3081-3095.
- 1402 Sterner, R.W., Andersen, T., Elser, J.J., Hessen, D.O., Hood, J.M., McCauley, E., Urabe, J., 2008.
1403 Scale-dependent carbon : nitrogen : phosphorus seston stoichiometry in marine and
1404 freshwaters. *Limnol. Oceanogr.*, 53(3): 1169-1180.
- 1405 Sylvan, J.B., Pyenson, B.C., Rouxel, O., German, C.R., Edwards, K.J., 2012. Time-series analysis of
1406 two hydrothermal plumes at 9 degrees 50'N East Pacific Rise reveals distinct, heterogeneous
1407 bacterial populations. *Geobiology*, 10(2): 178-192.
- 1408 Syverson, D.D., Borrok, D.M., Seyfried, W.E., 2013. Experimental determination of equilibrium Fe
1409 isotopic fractionation between pyrite and dissolved Fe under hydrothermal conditions.
1410 *Geochim. Cosmochim. Acta*, 122: 170-183.

- 1411 Syverson, D.D., Pester, N.J., Craddock, P.R., Seyfried, W.E., 2014. Fe isotope fractionation during
1412 phase separation in the NaCl-H₂O system: An experimental study with implications for
1413 seafloor hydrothermal vents. *Earth. Planet. Sci. Lett.*, 406: 223-232.
- 1414 Tagliabue, A., Bopp, L., Dutay, J.C., Bowie, A.R., Chever, F., Jean-Baptiste, P., Bucciarelli, E.,
1415 Lannuzel, D., Remenyi, T., Sarthou, G., Aumont, O., Gehlen, M., Jeandel, C., 2010.
1416 Hydrothermal contribution to the oceanic dissolved iron inventory. *Nature Geoscience*, 3(4):
1417 252-256.
- 1418 Templeton, A.S., Staudigel, H., Tebo, B.M., 2005. Diverse Mn(II)-oxidizing bacteria isolated from
1419 submarine basalts at Loihi Seamount. *Geomicrobiol. J.*, 22(3-4): 127-139.
- 1420 Teng, F.Z., Dauphas, N., Huang, S.C., Marty, B., 2013. Iron isotopic systematics of oceanic basalts.
1421 *Geochim. Cosmochim. Acta*, 107: 12-26.
- 1422 Tolstoy, M., Cowen, J.P., Baker, E.T., Fornari, D.J., Rubin, K.H., Shank, T.M., Waldhauser, F.,
1423 Bohnenstiehl, D.R., Forsyth, D.W., Holmes, R.C., Love, B., Perfit, M.R., Weekly, R.T.,
1424 Soule, S.A., Glazer, B., 2006. A sea-floor spreading event captured by seismometers. *Science*,
1425 314(5807): 1920-1922.
- 1426 Toner, B.M., Fakra, S.C., Manganini, S.J., Santelli, C.M., Marcus, M.A., Moffett, J., Rouxel, O.,
1427 German, C.R., Edwards, K.J., 2009. Preservation of iron(II) by carbon-rich matrices in a
1428 hydrothermal plume. *Nature Geoscience*, 2(3): 197-201.
- 1429 Toner, B.M., German, C.R., Dick, G.J., Breier, J.A., 2016. Deciphering the Complex Chemistry of
1430 Deep-Ocean Particles using Complementary Synchrotron X-ray Microscope and Microprobe
1431 Instruments. *Acc. Chem. Res.*, 49: 128-137.
- 1432 Toner, B.M., Marcus, M.A., Edwards, K.J., Rouxel, O., German, C.R., 2012. Measuring the Form of
1433 Iron in Hydrothermal Plume Particles. *Oceanography*, 25(1): 209-212.
- 1434 Toner, B.M., Nicholas, S.L., Coleman Wasik, J.K., 2014. Scaling up: Fulfilling the promise of X-ray
1435 microprobe for biogeochemical research. *Environmental Chemistry*, 11: 4-9.
- 1436 Trocine, R.P., Trefry, J.H., 1988. Distribution and chemistry of suspended particles from an active
1437 hydrothermal vent site on the Mid-Atlantic Ridge at 26 °N. *Earth. Planet. Sci. Lett.*, 88(1-2):
1438 1-15.
- 1439 Von Damm, K.L., 1988. Systematics of and postulated controls on submarine hydrothermal solution
1440 chemistry. *J. Geophys. Res.-Solid Earth*, 93(B5): 4551-4561.
- 1441 Von Damm, K.L., 2000. Chemistry of hydrothermal vent fluids from 9°–10°N, East Pacific Rise:
1442 "Time zero," the immediate post-eruptive period. *J. Geophys. Res.-Solid Earth*, 105(B5):
1443 11203-11222.
- 1444 Von Damm, K.L., 2004. Evolution of the hydrothermal system at East Pacific Rise 9 degrees 50 ' N:
1445 Geochemical evidence for changes in the Upper Oceanic Crust. In: German, C.R., Lin, J.,
1446 Parson, L.M. (Eds.), *Mid-Ocean Ridges: Hydrothermal Interactions between the Lithosphere
1447 and Oceans. Geophysical Monograph Series*, pp. 285-304.

- 1448 Von Damm, K.L., Buttermore, L.G., Oosting, S.E., Bray, A.M., Fornari, D.J., Lilley, M.D., Shanks,
1449 W.C., 1997. Direct observation of the evolution of a seafloor 'black smoker' from vapor to
1450 brine. *Earth. Planet. Sci. Lett.*, 149(1-4): 101-111.
- 1451 Von Damm, K.L., Edmond, J.M., Grant, B., Measures, C.I., Walden, B., Weiss, R.F., 1985. Chemistry
1452 of submarine hydrothermal solutions at 21°N, East Pacific Rise. *Geochim. Cosmochim. Acta*,
1453 49: 2197-2220.
- 1454 Von Damm, K.L., Oosting, S.E., Kozlowski, R., Buttermore, L.G., Colodner, D.C., Edmonds, H.N.,
1455 Edmond, J.M., Grebmeier, J.M., 1995. Evolution of East Pacific Rise hydrothermal vent fluids
1456 following a volcanic eruption. *Nature*, 375(6526): 47-50.
- 1457 Walsh, I., Fischer, K., Murray, D., Dymond, J., 1988. Evidence for resuspension of rebound particles
1458 from near-bottom sediment traps. *Deep Sea Res. (I Oceanogr. Res. Pap.)*, 35(1): 59-70.
- 1459 Wheat, C.G., Mottl, M.J., 2000. Composition of pore and spring waters from baby bare: Global
1460 implications of geochemical fluxes from a ridge flank hydrothermal system. *Geochim.*
1461 *Cosmochim. Acta*, 64: 629-642.
- 1462 Wu, J.F., Wells, M.L., Rember, R., 2011a. Dissolved iron anomaly in the deep tropical-subtropical
1463 Pacific: Evidence for long-range transport of hydrothermal iron. *Geochim. Cosmochim. Acta*,
1464 75(2): 460-468.
- 1465 Wu, L.L., Beard, B.L., Roden, E.E., Johnson, C.M., 2011b. Stable Iron Isotope Fractionation Between
1466 Aqueous Fe(II) and Hydrated Ferric Oxide. *Environ. Sci. Technol.*, 45(5): 1847-1852.
- 1467 Wu, L.L., Beard, B.L., Roden, E.E., Kennedy, C.B., Johnson, C.M., 2010. Stable Fe isotope
1468 fractionations produced by aqueous Fe(II)-hematite surface interactions. *Geochim.*
1469 *Cosmochim. Acta*, 74(15): 4249-4265.
- 1470 Wu, L.L., Druschel, G., Findlay, A., Beard, B.L., Johnson, C.M., 2012. Experimental determination of
1471 iron isotope fractionations among Fe-aq(2+)-FeSaq-Mackinawite at low temperatures:
1472 Implications for the rock record. *Geochim. Cosmochim. Acta*, 89: 46-61.
- 1473 Yucel, M., Gartman, A., Chan, C.S., Luther, G.W., 2011. Hydrothermal vents as a kinetically stable
1474 source of iron-sulphide-bearing nanoparticles to the ocean. *Nature Geoscience*, 4(6): 367-371.
- 1475 Yucel, M., Luther, G.W., 2013. Temporal trends in vent fluid iron and sulfide chemistry following the
1476 2005/2006 eruption at East Pacific Rise, 9 degrees 50 ' N. *Geochem Geophys Geosy*, 14(4):
1477 759-765.
- 1478
- 1479
- 1480

1481 **Table captions**

1482 **Table 1:** Temperature, pH and chemical and Fe isotope composition of the hydrothermal
1483 fluids at 9°50'N EPR. Individual data obtained for the dissolved (Diss) and particulate fraction
1484 (Dregs) are also shown.

1485 **Table 2:** Time series of mass flux and geochemical composition of plume particulates
1486 collected in sediment traps at 9°50'N EPR.

1487 **Table 3:** Average mass flux and geochemical composition of plume particulate collected in
1488 sediment traps at 9°50'N EPR and other locations.

1489 **Table 4:** Summary of sediment trap samples analyzed using Fe XANES spectroscopy and
1490 corresponding Fe species bins (mol %) obtained from linear combination fitting of
1491 experimental spectra with references.

1492 **Table 5:** End-member chemical composition of the different components used for
1493 geochemical modeling

1494 **Table 6:** Mass fluxes, Fe distribution and Fe isotope composition of the different components
1495 of plume particles determined by geochemical modeling. Only average data are presented.

1496

1497

1498 **Supplementary materials:**

1499 **Table S1.** Summary of all linear combination fit results for Fe XANES data from samples
1500 listed in Table 4. Variables P1, P2, and P3 represent that best fit mol fraction. Variables C1,
1501 C2, and C3 represent the best fit component as listed by the reference standard. The sum is
1502 the mol fraction component sum. The NSS is the normalized sum square parameter. Key to
1503 reference standard naming is provided in Table BMT-S2.

1504 **Table S2.** List of reference standards used in final best linear least squares fits to Fe XANES
1505 data. Component names and the Fe category or bin represented by each component
1506 represents are described.

1507

1508 **Figure captions**

1509 **Figure 1:** Bathymetric map of the East Pacific Rise study area near 9°50'N modified from
1510 Fornari et al. (2012). Red dots indicate the location of high-temperature vents active that
1511 remained active through the 2005/2006 eruption, and are labeled at right. The estimated
1512 extent of 2005–2006 lava flows between 9°47.5' and 9°55.7'N is shown as a blue line, based
1513 on Soule et al. (2007). Sediment trap locations are shown as inverted triangles.

1514 **Figure 2:** Chemical compositions and elemental ratios of plume particulates collected in
1515 sediment traps at 9°50'N EPR. Linear regression lines for the entire sample set are shown in
1516 plots (a), (c), (e) while regression lines for the < 1 mm and > 1 mm size fractions have been
1517 distinguished in plots (b), (d), (f).

1518 **Figure 3:** Chemical compositions and elemental ratios of plume particulates collected in
1519 sediment traps at 9°50'N EPR. Linear regression lines for the entire sample set are shown in
1520 plots (b), (d), (e) while regression lines for Reset traps (Bio9 and Tica), and for the R1 and R2
1521 traps have been distinguished from each other in plots (a), (c), (f). Large square symbol
1522 correspond to the composition of basaltic glass measured in recent lava flows at 9°50'N EPR
1523 (Goss et al., 2010). Red cross correspond at the composition of suspended particles of the
1524 nonbuoyant plume collected in November 2007 (Breier et al., 2012).

1525 **Figure 4:** Chemical compositions and elemental ratios of plume particulates collected in
1526 sediment traps at 9°50'N EPR. Linear regression lines for the entire sample set are shown in
1527 each plot. Dashed lines in plot (d) correspond to theoretical mixing lines between basaltic
1528 glass (black square symbol) and pure hydrothermal components (defined at Al/Fe=0). In order
1529 to explain the entire variability of the composition of plume particles, two hydrothermal
1530 components should be considered, one having $\delta^{56}\text{Fe}$ values lighter (down to 1.2‰) than the
1531 hydrothermal vent fluid values (about -0.4‰), consistent with sulfide-rich particles, and the
1532 other having heavier $\delta^{56}\text{Fe}$ values or heavier (up to -0.2‰) consistent with Fe-oxyhydroxide-
1533 rich particles.

1534 **Figure 5:** Plot of mass fluxes of plume particles (total), Fe-sulfides (FeS_2), volcanic material
1535 (Volc) and Fe-oxyhydroxides (FeOOH) for plume particulates collected in all sediment traps
1536 over a period of 170 days at 9°50'N EPR.

1537 **Figure 6:** Plot of mass fluxes of metalliferous sediment (SED), carbonate (CaCO₃), biogenic
1538 silica (Bio SiO₂) and organic matter (orgC) for plume particulates collected in all sediment
1539 traps over a period of 170 days at 9°50'N EPR.

1540 **Figure 7:** Plots of Fe isotope composition in bulk plume particulates and in the proportions of
1541 Fe present in volcanic (volc) and Fe sulfide (FeS₂) fractions in all sediment trap samples
1542 collected over a period of 170 days at 9°50'N EPR. Gray bar corresponds to the Fe isotope
1543 composition of high-temperature hydrothermal fluids at the adjacent Bio9 vent [Rouxel et al.,
1544 2008].

1545 **Figure 8:** Plot of Fe isotope composition in plume particulates corrected for the contribution
1546 from volcanic materials, and the relative proportion of Fe in metalliferous sediments (SED)
1547 and Fe-oxhydroxides (FeOOH). Hydrothermal components are determined as the sum of
1548 FeOOH and Fe-sulfides (FeS₂) in all sediment traps collected over a period of 170 days at
1549 9°50'N EPR. Gray bar corresponds to the Fe isotope composition of high-temperature
1550 hydrothermal fluids at Bio9

1551

Figure1

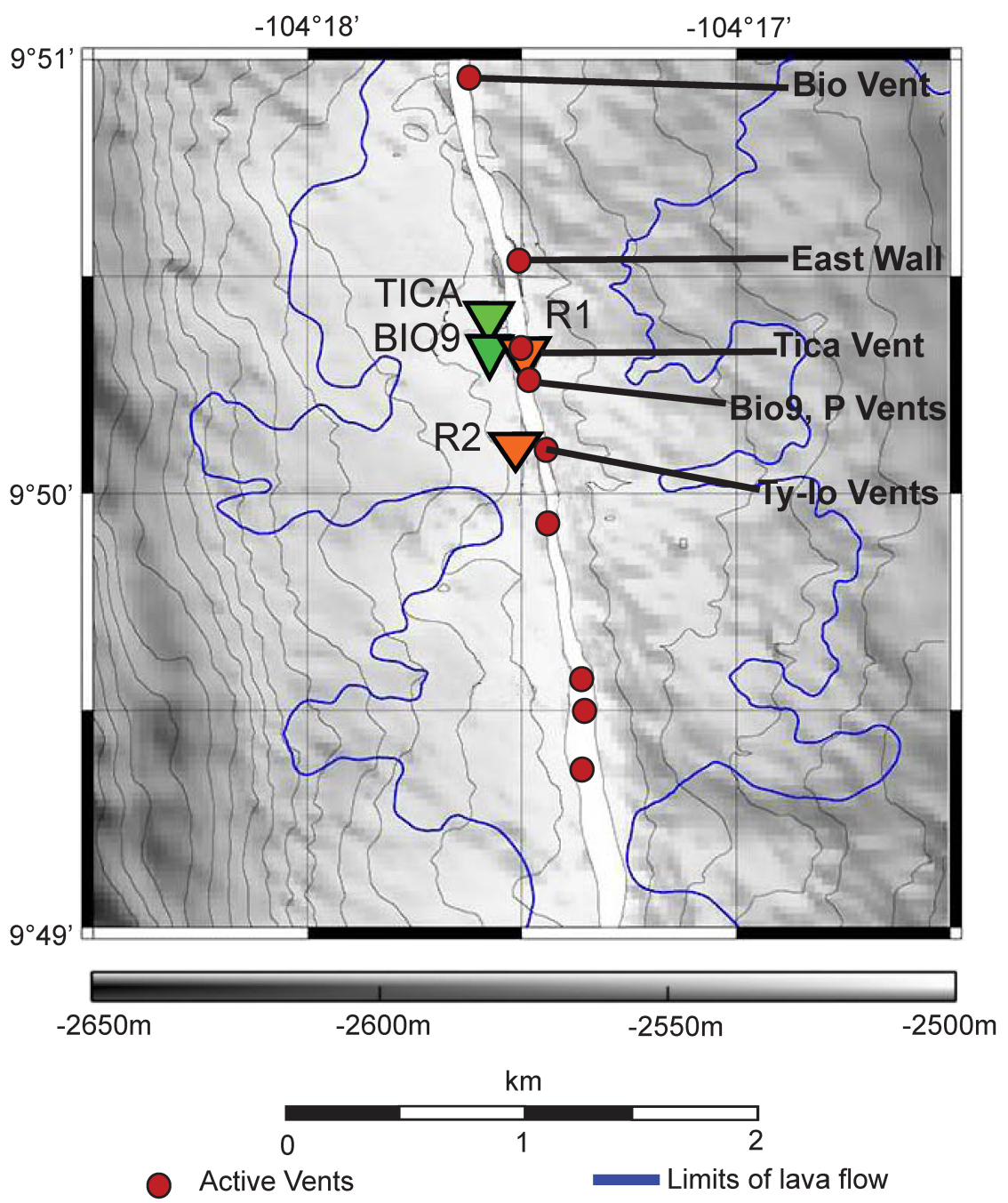


Figure 1

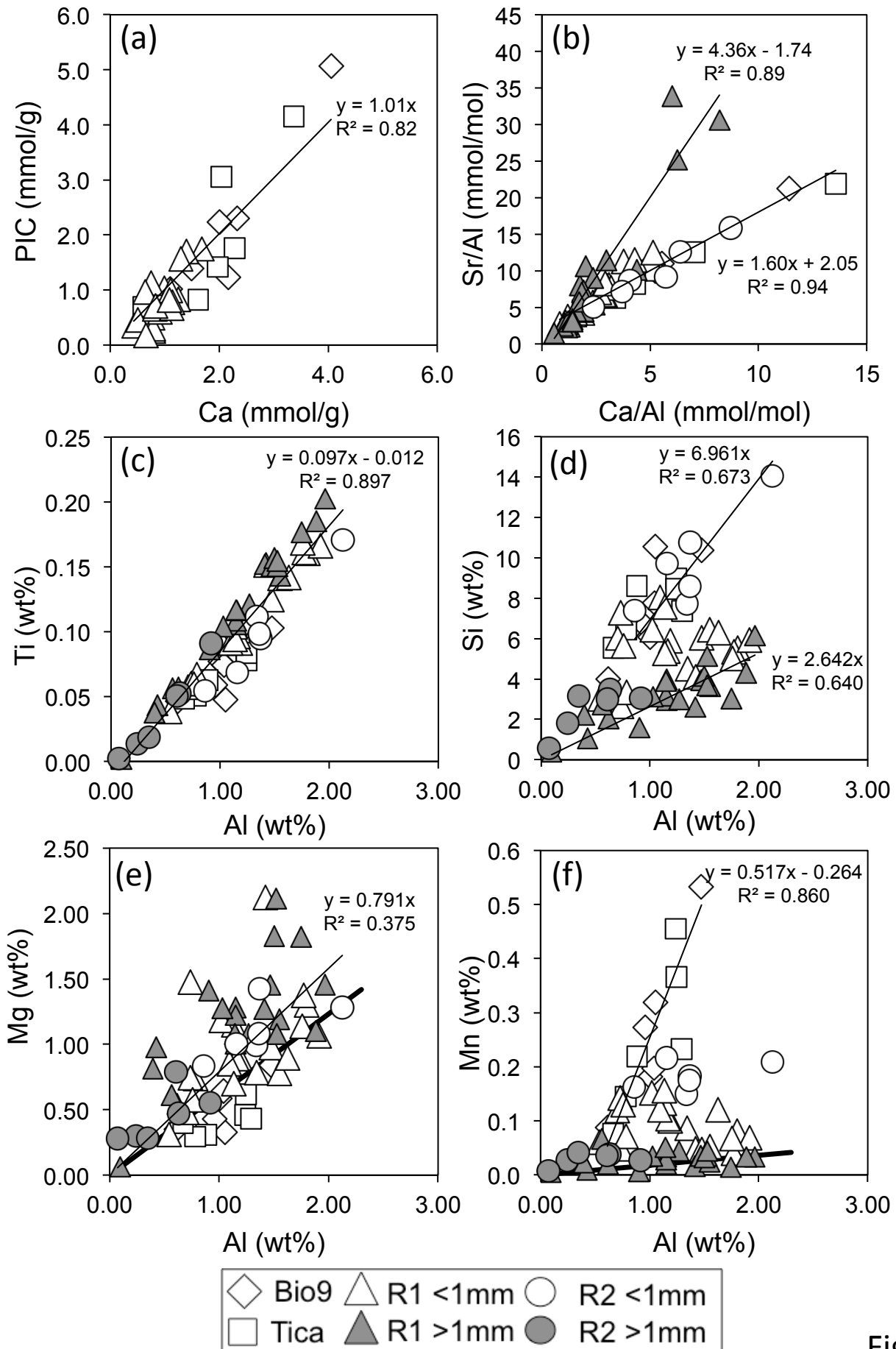


Figure 2

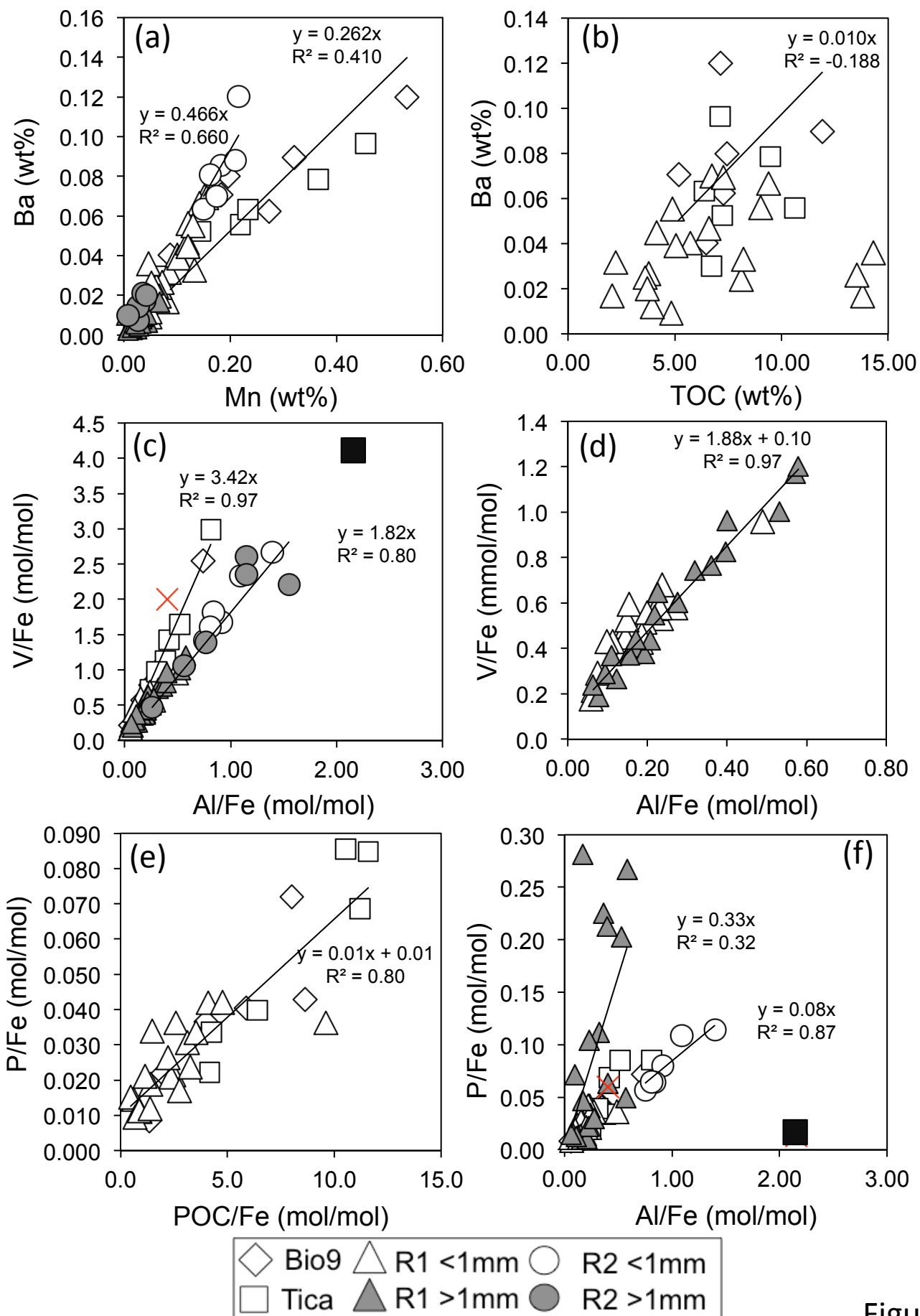


Figure 3

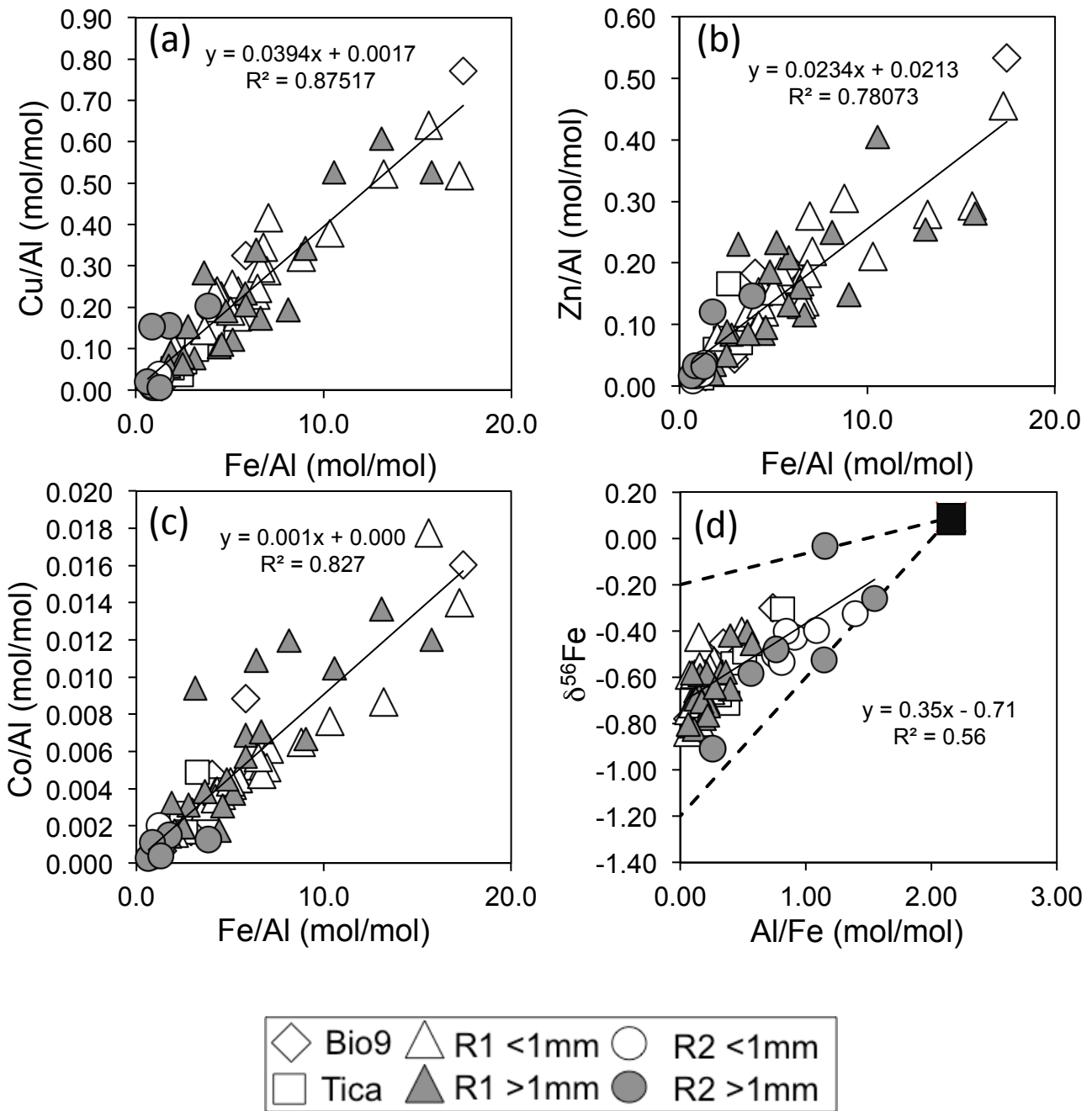


Figure 4

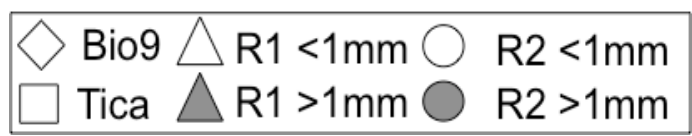
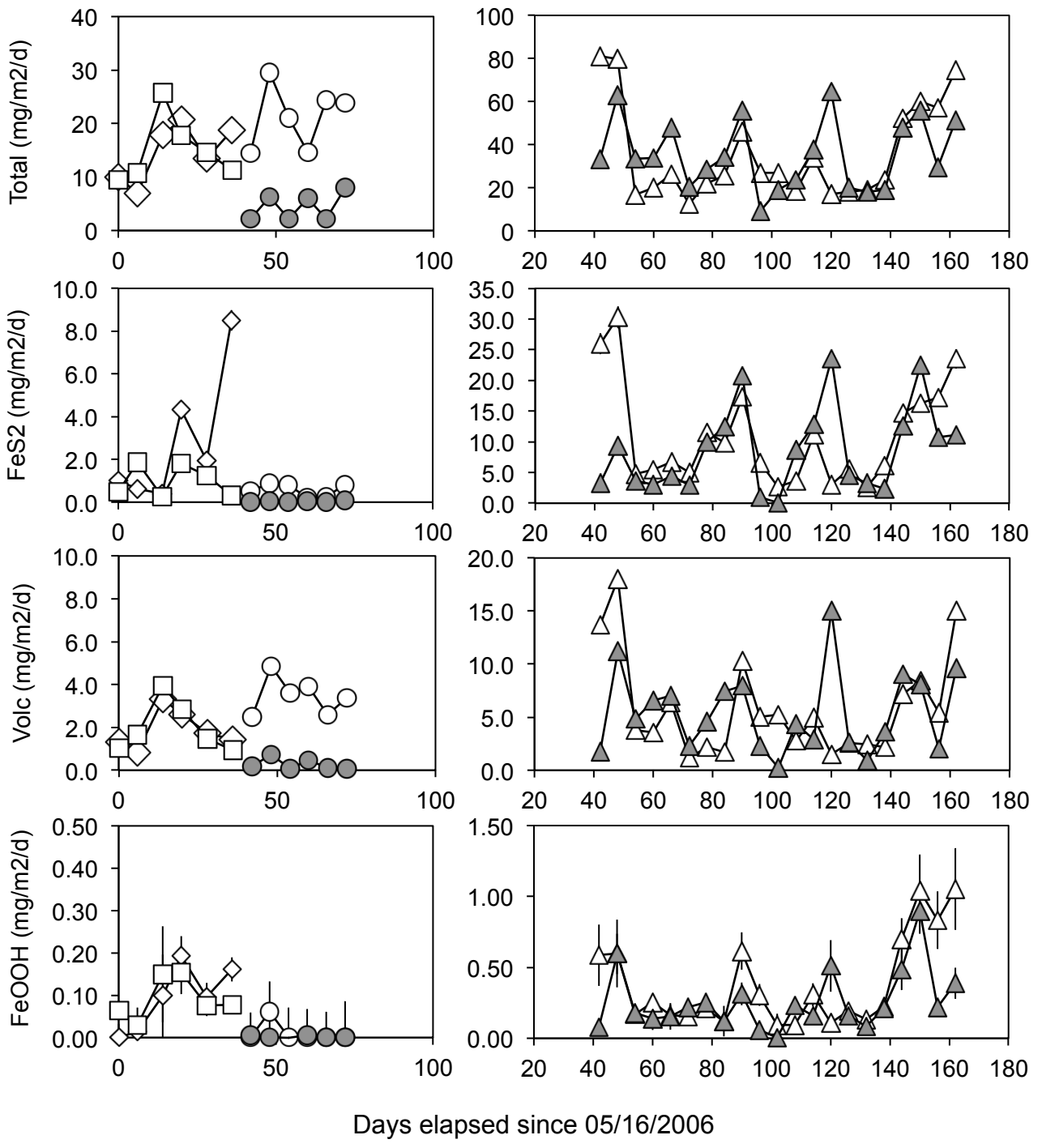


Figure 5

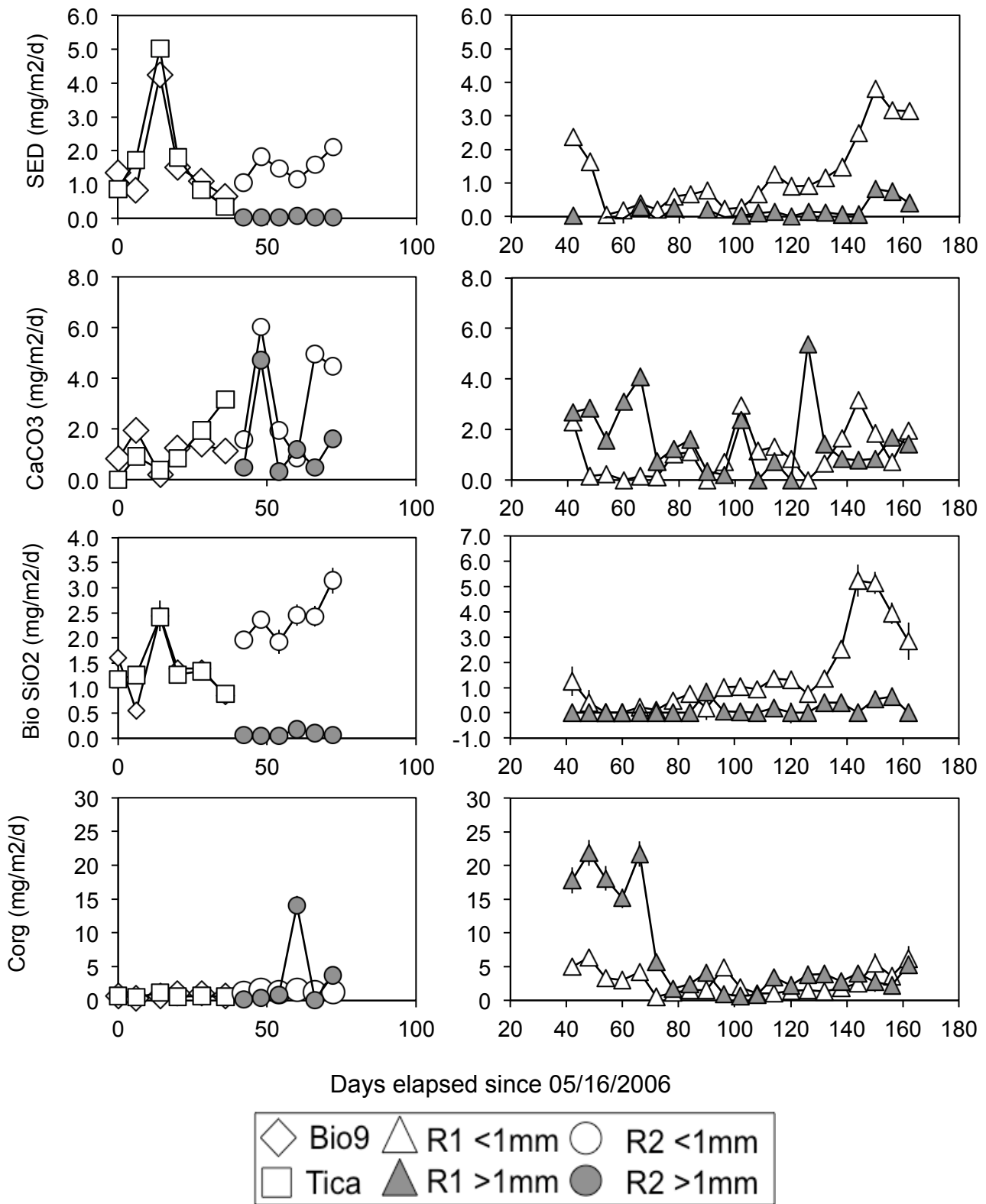


Figure 6

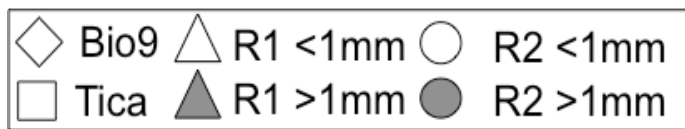
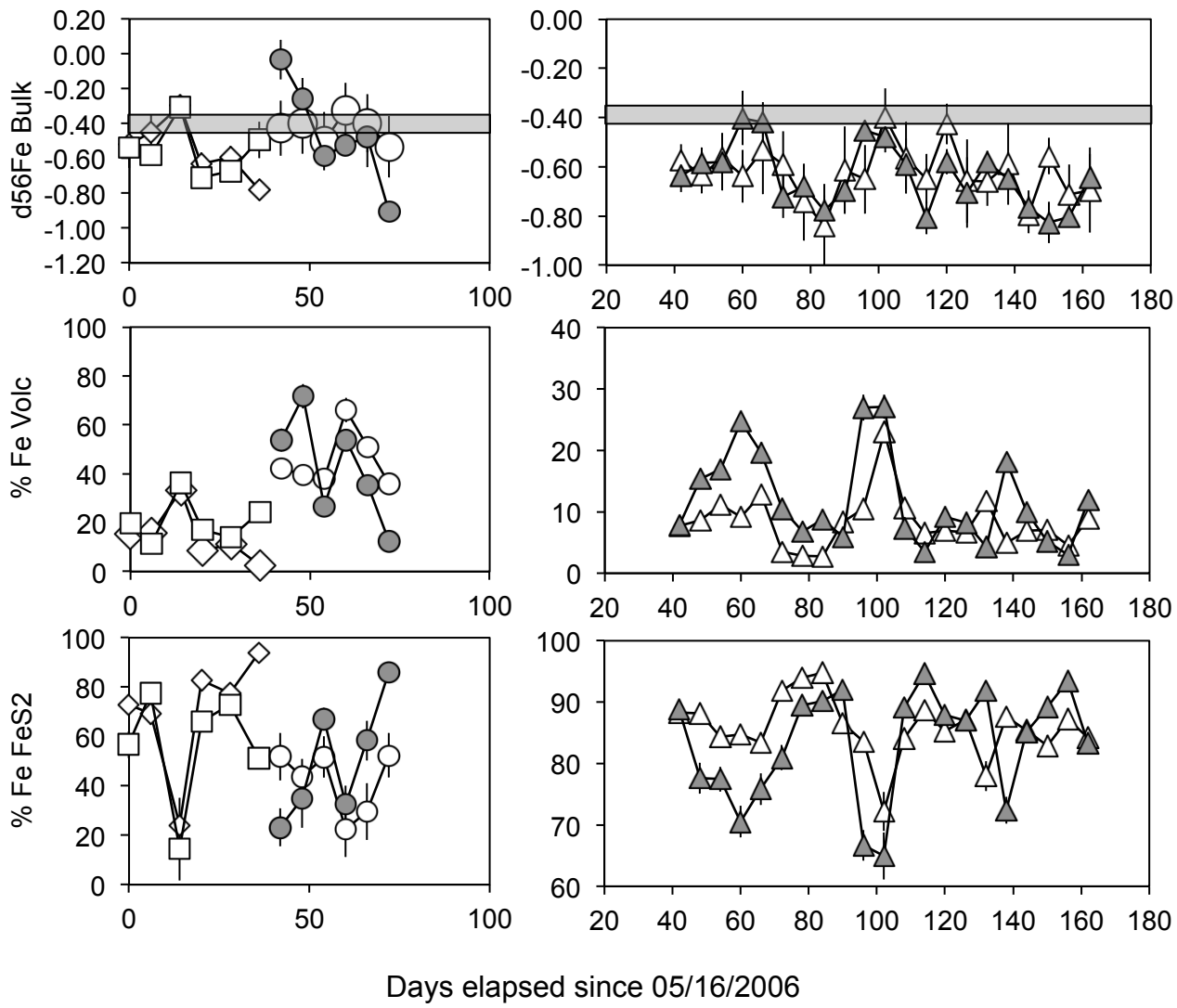


Figure 7

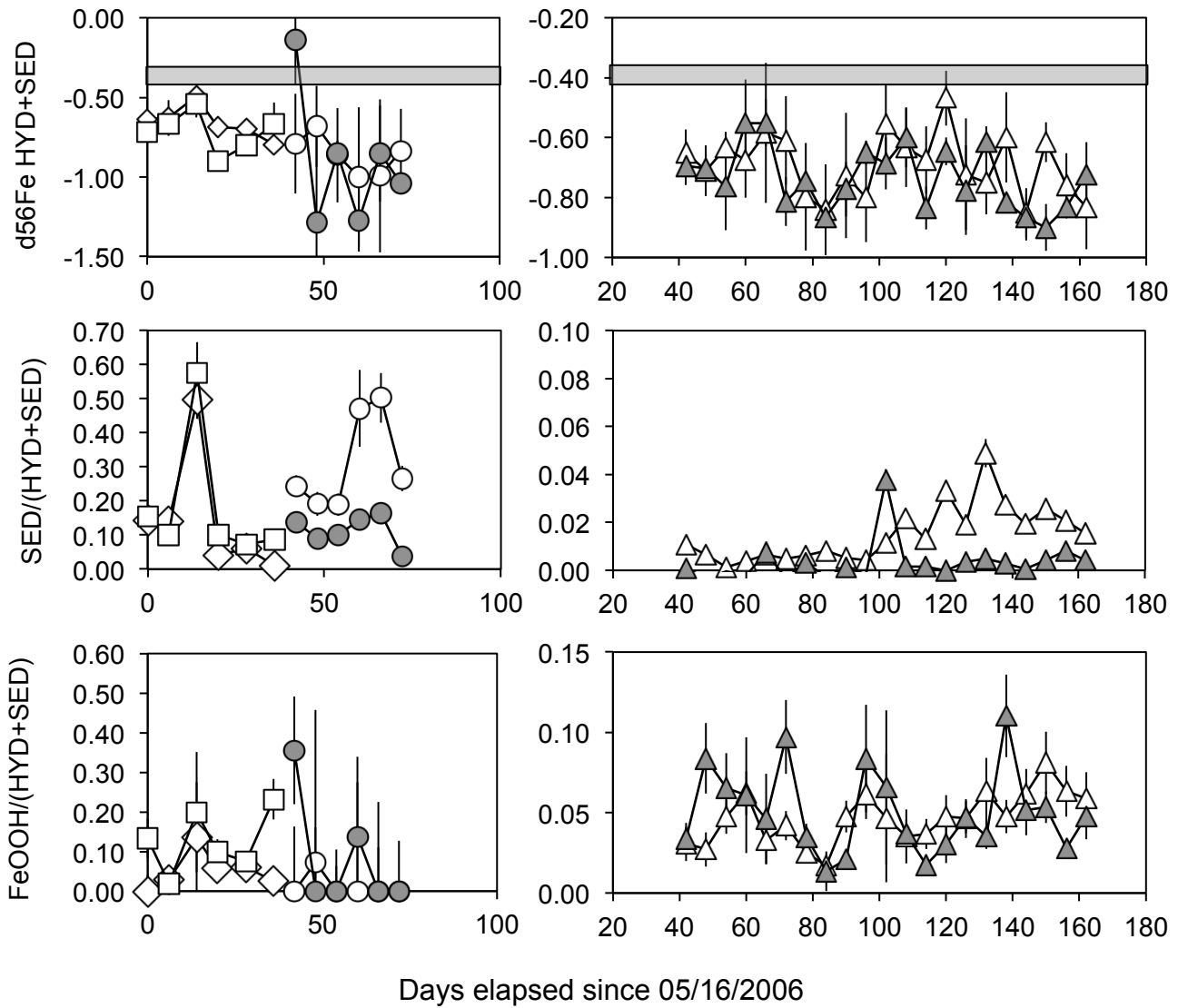


Figure 8

Table1

Table 1: Temperature, pH and chemical and Fe isotope composition of the hydrothermal fluids at 9°50'N EPR. Individual data obtained for the dissolved (Diss) and particulate fraction (Dregs) are also shown.

Sample	Sampling date (a)	T (°C) (b)	pH (25°C, 1atm)	Mg (mM)	Na (mM)	Fe (mM)	Mn (mM)	Cu (mM)	Zn (mM)	$d^{56}\text{Fe}$ 2sd	Fe EM (mM) (e)	$d^{56}\text{Fe EM}$ (f)	2sd	
ALV-4386-IGT1/Diss (c)				1.97		2699	578.4	0.4	10.5	-0.45	0.13			
ALV-4386-IGT1/Dregs (d)						34	0.9	16.9	78.7	-0.43	0.04			
ALV-4386-IGT1/Total	P-vent	01/02/2008	310	3.12	1.97	313	2733	579.3	17.3	89.2		2835	-0.45	0.13
ALV-4393-IGT5/Diss						3129	600.9	33.3	69.0	-0.40	0.07			
ALV-4393-IGT5/Dregs						151	0.8	103	45.2	-0.59	0.07			
ALV-4393-IGT5/Total	P-vent	01/08/2008	360	3.61	1.99	331	3280	601.7	136.5	114.2		3404	-0.41	0.07
ALV-4395-IGT6/Diss						2838	563.4	18.6	41.3	-0.36	0.12			
ALV-4395-IGT6/Dregs						42	0.4	22.6	12.5	-0.31	0.02			
ALV-4395-IGT6/Total	P-vent	01/10/2008	374	3.4	5.31	339	2880	563.8	41.2	53.8		3189	-0.36	0.12
ALV-4057-W1/Diss						3165	483	50.33	71.49	-0.43	0.05			
ALV-4057-W1/Dregs						8	0.14	2.85	3.65	-0.56	0.04			
ALV-4057-W1/Total	Bio9	11/20/2004	383	3.21	5.30	307	3173	483.1	53.2	75.1		3513	-0.43	0.05
ALV-4057-W2/Diss						3045	461	45.79	53.55	-0.38	0.07			
ALV-4057-W2/Dregs						43	0.15	16.70	19.83	-0.45	0.07			
ALV-4057-W2/Total	Bio9	11/20/2004	383	3.30	8.50	318	3088	461.2	62.5	73.4		3655	-0.38	0.07
ALV-4386-IGT6/Diss						2456	382.5	8.6	23.9	-0.42	0.09			
ALV-4386-IGT6/Dregs						316	0.6	168	23.3	-0.44	0.11			
ALV-4386-IGT6/Total	Bio9	01/01/2008	330	3.23	1.83	268	2772	383.1	176.5	47.1		2868	-0.42	0.09
ALV-4395-IGT5/Diss						2459	388.9	21.9	58.4	-0.40	0.10			
ALV-4395-IGT5/Dregs						32	0.6	12.0	22.1	-0.45	0.02			
ALV-4395-IGT5/Total	Bio9	01/10/2008	332	3.37	2.93	277	2491	389.4	33.9	80.4		2632	-0.40	0.10
ALV-4059-W1/Diss						1365	377	8.45	40.97	-0.33	0.18			
ALV-4059-W1/Dregs						52	0.23	2.98	14.14	-1.71	0.07			
ALV-4059-W1/Total	Tica	06/26/2005	344	3.16	5.20	228	1417	377.0	11.4	55.1		1565	-0.38	0.17
ALV-4059-W2/Diss						1282	369	7.45	39.31	-0.22	0.05			
ALV-4059-W2/Dregs						99	0.30	3.33	15.73	-1.79	0.05			
ALV-4059-W2/Total	Tica	11/22/2004	344	3.13	7.20	238	1381	369.3	10.8	55.0		1590	-0.33	0.05
ALV-4393-IGT6/Diss						411	81.0	0.1	10.8	-0.18	0.10			
ALV-4393-IGT6/Dregs						172	0.3	129	8.4	-0.33	0.14			
ALV-4393-IGT6/Total	Ty-lo	01/08/2008	300	3.8	2.48	146	583	81.3	128.6	19.2		611	-0.22	0.11
ALV-4061-W3/Diss						151	101	8.45	19.85	-0.64	0.11			
ALV-4061-W3/Dregs						5	0.10	1.43	2.84	-0.72	0.10			
ALV-4061-W3/Total	Biovent	11/24/2004	331	4.45	25.3	389	156	100.80	9.88	22.69		290	-0.64	0.11
ALV-4061-W4/Diss						264	180	12.34	27.00	-0.69	0.16			
ALV-4061-W4/Dregs						1	0.10	0.59	1.11	-0.72	0.22			
ALV-4061-W4/Total	Biovent	11/24/2004	331	3.79	4.3	320	266	180.46	12.93	28.11		289	-0.69	0.16

(a) 2008 data from Pester et al., 2014; 2004 data from Rouxel et al., 2008

(b) Maximum temperature measured using ICL temperature probe prior fluid sampling

(c) Diss: dissolved fraction recovered from Ti-sampler and acidified

(d) Dregs: insoluble particles precipitated inside the Ti-sampler

Table3

Table 3: Average mass flux and geochemical composition of plume particulate collected in sediment traps at 9°50'N EPR and other locations.

Traps	Total days	$\delta^{56}\text{Fe}$	CaCO ₃	TOC	Fe	Al	Mn	P	V	Cu	Zn	Mass flux	CaCO ₃ flux	TOC flux	Fe flux	Al flux	Mn flux	P flux	V flux	Cu flux	Zn flux	
			(wt%)				(mg/g)						(mg/cm ² /yr)	(mg/cm ² /yr)								
BIO9	(a)	-0.55	21.97	7.57	9.87	1.02	2655	1458	63	4602	3358	0.53	102.86	37.98	58.3	5.45	1.38	0.78	0.03	2.84	2.05	
BIO9	(b)	42.0	-0.64	19.58	7.01	10.80	1.02	2512	1466	64	5381	3880	0.53	103.41	37.03	57.0	5.39	1.33	0.77	0.03	2.84	2.05
TICA	(a)	-0.55	19.83	7.92	5.51	1.02	2489	1366	62	1670	2136	0.55	106.78	41.43	28.5	5.81	1.51	0.75	0.04	0.83	1.12	
TICA	(b)	42.0	-0.59	19.49	7.57	5.51	1.07	2712	1352	66	1661	2244	0.54	105.83	41.11	29.9	5.82	1.47	0.73	0.04	0.90	1.22
R1<1mm	(a)	-0.62	9.19	6.55	15.62	1.22	928	1850	65	7587	5148	1.32	122.39	72.47	215.2	17.11	1.29	2.35	0.09	10.08	7.02	
R1<1mm	(b)	126.0	-0.64	9.29	5.50	16.34	1.30	983	1786	69	7654	5330	1.32	122.39	72.47	215.2	17.11	1.29	2.35	0.09	10.08	7.02
R1>1mm	(a)	-0.64	9.45		12.07	1.16	293	3191	52	5202	3879	1.30	111.69		170.2	15.90	0.39	4.18	0.07	7.21	5.84	
R1>1mm	(b)	126.0	-0.68	8.60		13.11	1.22	302	3219	54	5558	4497	1.30	111.69		170.2	15.90	0.39	4.18	0.07	7.21	5.84
R2<1mm	(a)	-0.59	24.93		2.86	1.31	1892	1243	49	786	679	0.81	207.28		23.2	10.21	1.50	0.97	0.04	0.62	0.56	
R2<1mm	(b)	36.0	-0.43	25.54		2.85	1.26	1853	1193	48	768	685	0.81	207.28		23.2	10.21	1.50	0.97	0.04	0.62	0.56
R2>1mm	(a)	-0.55	31.95		1.07	0.43	325	7981	14	1218	438	0.17	59.28		1.7	0.76	0.05	1.69	0.00	0.19	0.07	
R2>1mm	(b)	36.0	-0.53	35.03		1.01	0.45	278	9981	14	1130	404	0.17	59.28		1.7	0.76	0.05	1.69	0.00	0.19	0.07
13°N / T4	(c)		5.5	6.2	11	0.3	590	2100	25	810	####	6.72	370	416	739	20	4	14	0.17	5	169	
13°N / T5	(c)		5.8	4.2	21	0.3	1900	2700	84	1800	####	16.2	940	679	3400	49	31	44	1.36	29	567	
13°N / T6	(c)		1.3	8.7	2.5	9.4	2900	2300	79	490	690	3.16	41	276	79	297	9.2	7.3	0.25	1.55	2.18	
13°N / T7	(c)		32.5	12.3	0.3	2	360	1700	36	300	1300	1.96	637	240	5.9	39	0.7	3.3	0.07	0.59	2.55	
13°N / T8	(c)		50	12.9	0.6	0.4	21	1600	27	440	340	2.45	1220	317	15	10	0.1	3.9	0.07	1.08	0.83	
Endeavour	(d)	336										2.44	612	92	218	31.4	3.37		3.51	14.6	44.9	
ALOHA	(e)											0.72		0.17	6.64	9.03	0.18			0.05		
BATS	(f)													11.94				0.88	0.05	0.13	0.25	

(a) arithmetic mean; (b) weighted mean; (c) Data from East Pacific Rise à 13°N (German et al., 2003); (d) Data from Endeavour ridge, 2100m depth (Dymond et al., 1988)
(e) mass flux data from the North Equatorial Pacific (Lamborg et al., 2008); (f) mass flux data from the Bermuda Atlantic Time-series Study (BATS) station (Jickells et al., 1998)

Table 4: Summary of sediment trap samples analyzed using Fe XANES spectroscopy and corresponding Fe species bins (mol %) obtained from linear combination fitting of experimental spectra with references.

Sample Name	Number of XANES observations	Fe(III) oxyhydroxide + organics	silicates	Fe(II) oxides + glasses	Fe(III) phyllosilicate	Fe sulfides	
Bio9-16	18	5	3	8	40	43	(a)
Bio9-19	19	9	6	3	5	77	(a)
R1-16	9	5	0	4	2	89	(a)
R2-05	24	60	4	16	7	13	(b)
R2-07	16	63	7	4	22	4	(a)
R2-10	13	45	8	12	8	28	(b)
Tica-01	3	22	0	0	15	62	(a)
Tica-19	8	3	20	27	2	47	(c)

References: (a) this study; (b) Toner et al., 2012; 2013; (c) Toner et al., 2009

Table 5: End-member chemical composition of the different components used for geochemical modeling

		Al	Si	Ca	Sr	Mn	P	Cu+Zn	Fe	Ba	V
		(mg/g)									
FeOOH	(a)	0.00	0.0	0.0	0.00	0.00	44.06	0.00	661.5	0.00	1.81
	+/-	-	-	-	-	-	22.03	-	-	-	0.60
FeS2	(b)	0.00	0.0	0.0	0.00	0.00	0.00	35.18	465.8	0.00	0.00
	+/-	-	-	-	-	-	-	1.48	-	-	-
Hyd Sed.	(c)	0.79	12.6	289.9	0.01	21.56	3.06	0.34	57.5	1.40	0.16
	+/-	0.09	1.2	9.0	0.00	3.29	0.70	0.27	7.0	0.18	0.05
Volcanic	(d)	79.7	234.7	85.7	0.11	1.42	0.57	0.150	76.5	0.01	0.28
	+/-	0.5	0.9	1.1	0.00	0.08	0.07	0.003	1.2	0.00	0.07
Bio-CO3	(e)	0.00	0.0	400.5	1.40	0.00	0.00	0.00	0.0	0.00	0.00
	+/-	-	-	-	0.11	-	-	-	-	-	-
Bio-SiO2	(f)	0.00	467.5	0.0	0.00	0.00	0.00	0.00	0.0	0.00	0.00
	+/-	-	-	-	-	-	-	-	-	-	-
Corg	(g)	0.00	0.0	0.0	0.00	0.00	14.32	0.00	0.0	0.00	0.00
	+/-	-	-	-	-	-	1.43	-	-	-	-

(a) FeOOH: Fe-oxyhydroxides. Composition taken from published data of the non-boyant plume at EPR 9°50'N, V/Fe = 0.003 +/- 0.001 and P/Fe = 0.12 +/- 0.06 (Breier et al., 2012; Feely et al., 1994)

(b) FeS2: pyrite and other Fe-sulfides. Composition estimated from the correlation between Fe and Cu+Zn; with Fe/(Cu+Zn) = 13.24 +/- 0.6 (this study);

(c) Hyd Sed: Hydrothermal sediments. Composition taken from published data of South EPR sediment cores, average of last 200 ka (Mills et al., 2010);

(d) Volcanic: volcanic glass. Composition estimated from the average composition of volcanic glass from 2006 eruption, Axial central region (Goss et al., 2010);

(e) Bio-CO3: biogenic carbonate. Composition estimated using the correlation between Ca, Sr and TIC; Sr/Ca = 1.60 ± 0.12 (2se) mmol/mol (this study);

(f) Bio-SiO2: biogenic opale. Composition similar to pure opale;

(g) Corg: organic matter. Composition estimated from the correlation between P and C, with C/P of about 180 (mol/mol)

Table 6: Mass fluxes, Fe distribution and Fe isotope composition of the different components of plume particles determined by geochemical modeling. Only average data are presented.

Trap/fraction:	BIO9		TICA		R1 <1mm		R1 >1mm		R2 <1mm		R2 >1mm	
	Av.	1sd	Av.	1sd	Av.	1sd	Av.	1sd	Av.	1sd	Av.	1sd
Flux (mg/m²/d)												
Total	14.60	5.43	14.95	6.08	36.09	22.31	35.57	#####	21.34	5.93	4.48	2.60
Sediment	1.61	1.32	1.77	1.69	1.26	1.11	0.13	0.27	1.53	0.39	0.04	0.02
Volcanic	1.87	0.92	1.98	1.17	5.88	4.75	5.45	3.80	3.47	0.88	0.27	0.27
Bio-SiO ₂	1.37	0.65	1.39	0.52	1.47	1.58	0.15	0.25	2.38	0.44	0.08	0.05
Bio-CaCO ₃	1.13	0.59	1.21	1.16	1.05	0.96	1.61	1.38	3.31	2.12	1.46	1.67
FeOOH	0.09	0.08	0.09	0.05	0.38	0.31	0.26	0.21	0.01	0.03	0.00	0.00
Corg	0.75	0.27	0.69	0.23	2.83	1.85	6.73	7.23	1.35	0.18	3.21	5.50
FeS ₂	2.80	3.14	1.00	0.74	10.97	8.15	8.73	6.98	0.58	0.30	0.04	0.03
Distribution of Fe (%)												
FeOOH	4.1	3.0	9.3	5.4	4.3	1.5	4.3	2.1	0.7	1.8	3.7	6.5
FeS ₂	70.1	24.1	56.4	22.8	85.8	4.9	83.3	9.0	41.9	13.0	50.3	24.1
Sediment	10.9	11.3	12.9	11.1	1.4	1.1	0.3	0.6	15.2	4.5	6.0	2.9
Volcanic	14.4	10.4	20.5	9.0	8.4	4.4	12.0	7.6	45.4	11.4	42.2	21.6
Fe isotope composition												
$\delta^{56}\text{Fe}$ Bulk	-0.55	0.16	-0.55	0.15	-0.62	0.11	-0.64	0.13	-0.43	0.08	-0.47	0.30
$\delta^{56}\text{Fe}_{\text{HYD+SED}}$	-0.66	0.16	-0.72	0.15	-0.69	0.11	-0.73	0.13	-0.86	0.12	-0.91	0.42

Sediment: includes potential hydrothermal Mn-rich sediments; Bio-SiO₂: biogenic opale; Bio-CO₃: biogenic carbonate; FeOOH: Fe-oxyhydroxides; Corg: organic matter; FeS₂: pyrite and other Fe-sulfides
 $\delta^{56}\text{Fe}_{\text{HYD+SED}}$: Fe isotope compositions of plume particles corrected for volcanic components